TABLE DES MATIÈRES

Page

LISTE DES TABLEAUX

Page

LISTE DES FIGURES

Page

LISTE DES ABRÉVIATIONS, SIGLES ET ACRONYMES

MIM	Moulage par injection des poudres métalliques (*metal injection molding*)
PIM	Moulage par injection des poudres (*powder injection molding*)
LPIM	Moulage à basse pression des poudres métalliques (*low-pressure metal injection molding*)
HPIM	Moulage à haute pression des poudres métalliques (*high-pressure metal injection molding*)
vol. %	Pourcentage volumique
wt. %	Pourcentage massique
SEM	Microscopie électronique à balayage
DSC	Calorimétrie différentielle à balayage
TGA	Analyse thermogravimétrique
CW	Cire de Carnauba
EVA	Éthylène-vinyle acétate
SA	Acide stéarique
PW	Cire de paraffine
ϕ	Fraction volumique de poudre

LISTE DES SYMBOLES ET UNITÉS DE MESURE

A	Diamètre des particules (μm)
E	Énergie d'activation (J/mol)
R	Constante des gaz parfaits ($J \cdot kg^{-1} \cdot K^{-1}$)
T	Température (°C)
P	Pression (MPa)
K	Conductivité thermique ($w \cdot m^{-1} \cdot K^{-1}$)
n	Coefficient de sensibilité au cisaillement du mélange
t	Temps (s)
V	Vecteur de vitesse (mm/s)
α_{STV}	Indice de moulabilité
$\dot{\gamma}$	Taux de cisaillement (s^{-1})
η	Viscosité du mélange (Pa·s)
ρ	Densité des particules (g/cm)
τ	Tenseur de contrainte visqueuse
g	Accélération de pesanteur (m/s^2)
η_0	Viscosité de référence (Pa·s)

INTRODUCTION

Ce rapport présente le projet de recherche élaboré durant deux ans au Laboratoire d'optimisation des procédés de fabrication avancée à l'École de technologie supérieure de Montréal. Le sujet porte sur l'injection des poudres métalliques à basse pression. Ce jeune procédé de mise en forme permet la production de pièces très complexe géométriquement avec un coût réduit. Il est de plus en plus utilisé dans le domaine de l'aérospatiale, et biomédicale et possède un fort potentiel pour une expansion dans les domaines de l'automobile et le militaire.

Le procédé d'injection des poudres métallique à basse pression (LPIM) implique la préparation de la matière première en mélangeant une poudre métallique avec un liant fondu, qui est injecté dans une cavité de moule. Après la solidification du liant, une pièce est formée qui est ensuite délianté et finalement frittée pour éliminer complètement le liant et obtenir une pièce métallique dense. Ce projet de recherche traite spécifiquement de la phase d'injection afin de mieux comprendre et interpréter le comportement des mélanges poudres-liants existants et en développement. L'utilisation d'un outil de simulation numérique a permis de prédire le comportement des mélanges pendant le remplissage d'un moule puis des injections à l'échelle réelle ont permis de valider expérimentalement les prédictions du modèle numérique. Notons que la simulation numérique de tel mélange métallique à base de cire a été réalisée pour la première fois dans le cadre de cette étude. Dans ce projet, les caractéristiques des mélanges ont été obtenu expérimentalement puis introduites dans le logiciel d'analyse Autodesk Moldflow Synergy 2019. Tous les résultats de simulation numérique ont été validés expérimentalement.

Le premier chapitre est orienté vers une revue de la littérature sur le moulage par injection des poudres métalliques afin de le contextualiser parmi les autres techniques de fabrication de pointe. Aussi, les différents modèles disponibles dans la littérature sont exposés puis les équations utilisées par le progiciel Autodesk Moldflow Synergy 2019 sont présentées. Le second chapitre présente la problématique et les objectifs de cette recherche. Ensuite, le troisième chapitre est consacré à la méthodologie utilisée pour chercher les caractéristiques des

mélanges étudiés. Par la suite, les quatrième et cinquième présente deux articles scientifiques. Le premier article de journal traite de l'effet de la forme et la taille de la poudre sur les propretés rhéologiques, thermiques, et sur l'homogénéité des mélanges pour l'injection des poudres métallique à basse pression (soumis dans *Journal of Materials Engineering and Performance, Springer*). Le deuxième article de journal présente notre deuxième article de journal à propos de la simulation de la phase d'injection avec une validation expérimentale en traitant le défaut de la ségrégation des poudres (sera soumis dans *Journal of Materials Processing Technology, Elsevier*). Enfin une conclusion avec un résumé des principaux résultats trouvés avec quelques recommandations pour l'orientation des futurs travaux de recherche.

CHAPITRE 1

REVUE DE LA LITTÉRATURE

Le premier chapitre de ce mémoire présente le procédé d'injection des poudres métalliques suivit d'une explication des notions de simulation numérique de la phase d'injection.

1.1 Moulage par injection des poudres métalliques

L'injection des poudres métalliques (ou en anglais *Metal Injection Molding*, dénoté pour le reste de ce document par l'acronyme MIM) est un procédé bien adapté pour la mise en forme des pièces métalliques de formes très complexes, précises et de faible taille (du millimètre à quelque dizaine de millimètres) faite à partir de matériaux à forte valeur ajoutée. Ce procédé est utilisé dans l'industrie automobile, médicale, aéronautique, militaire, joaillerie, électronique et beaucoup d'autres secteurs tel que montré à la Figure 1.1 (German & Bose, 1997). Ce procédé se distingue par la production de grande série de pièces avec une cadence similaire à celle de l'injection plastique (la notion de production rentable en faible série sera discutée plus bas à la section traitant du procédé de moulage des poudres à basse pression). Le procédé de l'injection des poudres métallique nous permet d'avoir des pièces avec des densités comparables à celle fournie par la fonderie mais avec une meilleure précision géométrique et surtout, une meilleure microstructure (granulaire) produisant de meilleures propriétés mécaniques. Le procédé MIM a été développé à partir de l'injection des polymères plastiques et comporte la flexibilité de l'injection plastique de point de vue géométrie et la précision géométrique de la métallurgie des poudres (Hausnerova, 2011).

Figure 1.1 Exemple de pièces produites par *MIM* (Leyens & Peters, 2003)

Le marché actuel de l'injection des poudres métallique se partage entre plusieurs continents et domaines. La plus grande partie du marché constitue les composants industriels avec 20 % principalement situé au Japon, 14 % pour les pièces automobiles en Europe, 11 % pour les produits électroniques en Asie, environ 9 % des produits médicaux et le reste du marché est occupé par d'autres domaines militaire, aérospatiale et joaillerie (Heaney, 2012).

1.1.1 Étapes du procédé MIM

L'injection des poudres métallique MIM est divisée en quatre étapes qui sont la préparation du mélange, l'injection, le déliantage et le frittage (Figure 1.2).

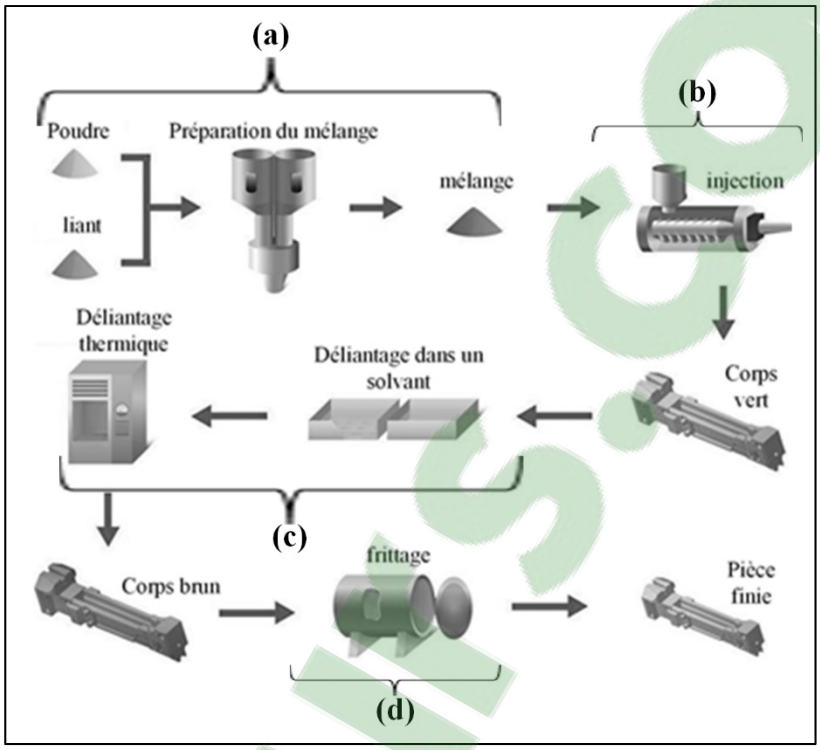

Figure 1.2 Les étapes du procédé MIM
(http://www.finemim.com/metal-injection-molding)

1.1.1.1 Préparation du mélange

La première étape consiste à combiner la poudre et le liant fondu dans un mélangeur jusqu'à l'obtention d'une répartition homogène des particules de poudre à travers le liant (Figure 1.2a). Le liant est généralement à base de thermoplastiques ou d'autres polymères tels que les cires naturelles (cire de carnauba et cire d'abeille) ou cires synthétiques (cire de paraffine et cire microcristalline) combiné à des constituants secondaires comme des agents tensioactifs (acide oléique, huile d'arachide, huile de poisson, stéarate de zinc, etc.) et des agents épaississants (éthylène-acétate de vinyle et polyéthylène basse densité). La matière première est généralement préparée entre 70 et 120 °C qui est supérieure au point de fusion du liant mais inférieur à la température de fusion de la poudre métallique. Le mélange de la poudre et du liant constituant la matière première du procédé d'injection est appelé mélange (ou en anglais *feedstock*). Il existe plusieurs techniques de fabrication de la poudre qui peuvent être utilisées pour produire des poudres de bonne qualité pour le MIM. Nicolas Giguère résume très bien les

différentes techniques d'atomisation où les deux techniques les plus utilisés sont l'atomisation au gaz et l'atomisation à l'eau (Giguère, 2010). Les poudres atomisées au gaz et à l'eau sont produites à partir d'un métal liquide qui est forcé à travers une buse jusqu'à un flux à haute de vitesse de gaz (généralement l'azote, l'argon ou l'hélium) ou d'eau briser le film de métal liquide en fines gouttelettes qui se solidifient puis tombe dans le fond de l'atomiseur tel qu'illustré à la Figure 1.3.

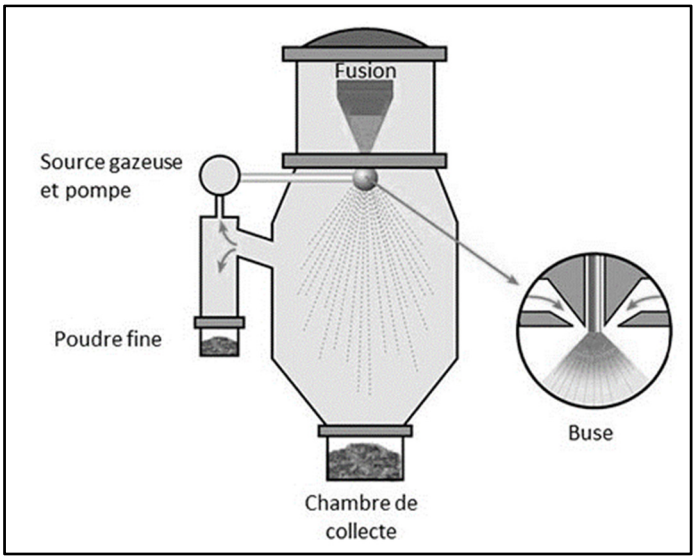

Figure 1.3 Atomiseur à gaz
(https://www.lpwtechnology.com/fr/technical-library/powder-production/)

Les poudres se classent par leurs granulométries (i.e., la distribution des particules) et leurs morphologies. La Figure 1.4 présente deux images prises par microscope électronique à balayage pour une poudre atomisée à gaz (Figure 1.4.a) et une poudre atomisée à l'eau (Figure 1.4.b). La poudre atomisée au gaz possède généralement une forme sphérique avec une rugosité de surface faible qui minimisent la friction interparticulaire lors de l'injection tandis que la poudre atomisée à l'eau se distingue par des particules qui ont généralement une forme irrégulière et un état de surface rugueux ce qui augmente la friction interparticulaire lors de l'injection diminuant ainsi le potentiel de moulage.

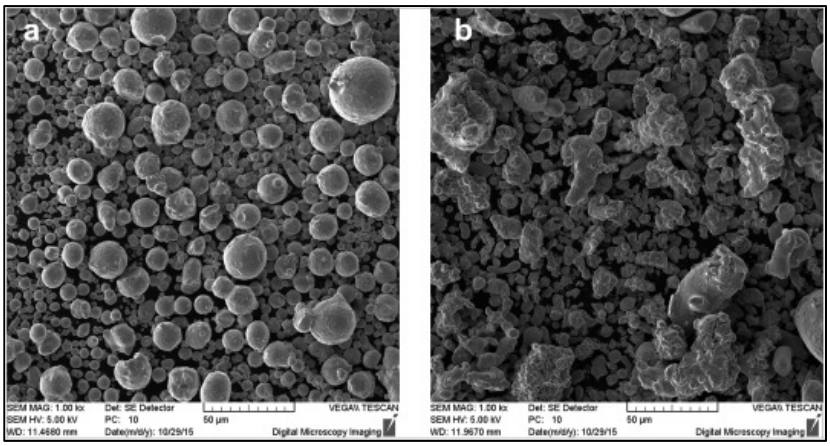

Figure 1.4 Images MEB de poudres atomisées (a) au gaz et (b) à l'eau (Hausnerova, Mukund, & Sanetrnik, 2017)

1.1.1.2 Injection

La seconde étape du procédé MIM est l'injection qui permet de générer la géométrie de la pièce (Figure 1.2b). Le processus commence par une alimentation de matière première en forme de granules à partir de la trémie qui fond par la suite à l'intérieur du cylindre pour dépasser la température de fusion du liant (Figure 1.5). Durant l'avance de la matière dans le cylindre par le mouvement de rotation de vis sans fin, la pression et la température de la matière augmente et le mélange ainsi fondu atteint la buse d'injection dans un état visqueux qui est ensuite injecté selon la séquence d'injection présentée en détail à la Figure 1.6.

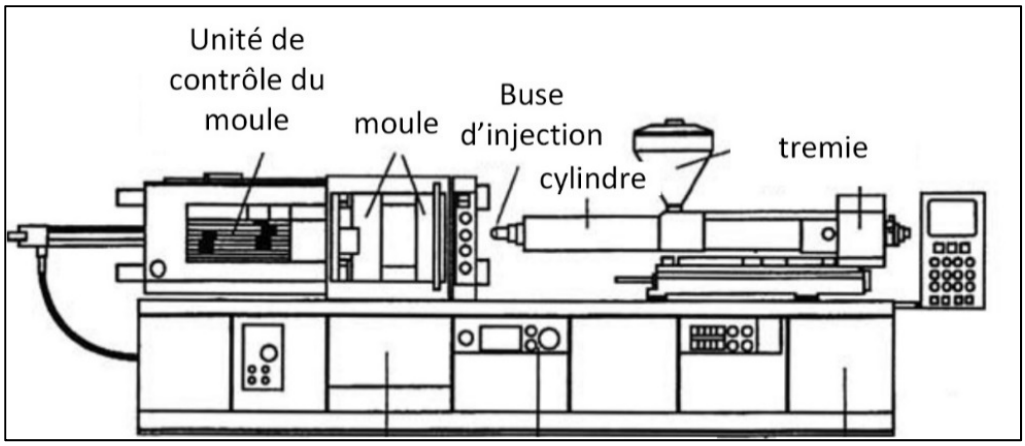

Figure 1.5 Presse d'injection (German, 2012)

Suite à la fermeture du moule, le mouvement du mélange est forcé à travers la cavité créant ainsi une pression d'injection (Figure 1.6). La vitesse d'injection est très importante pour garantir une pièce conforme aux attentes de l'industriel. Une vitesse très élevée peut générer une séparation de la poudre et du liant pour former une pièce non homogène. Une pièce avec des zones de concentration de poudre ou de liant génère une géométrie et des caractéristiques mécaniques non souhaitées à la suite de l'injection. Suite au remplissage complet, la pression est maintenu afin de combler le retrait de la pièce jusqu'à sa solidification finale puis son éjection du moule avant que le moule soit refermé pour l'injection suivante (Figure 1.6). Le refroidissement du moule est généralement effectué avec la circulation d'eau dans des circuits de refroidissement du moule. La pièce ainsi formée après l'injection est appelée corps vert (ou en anglais *geen part*).

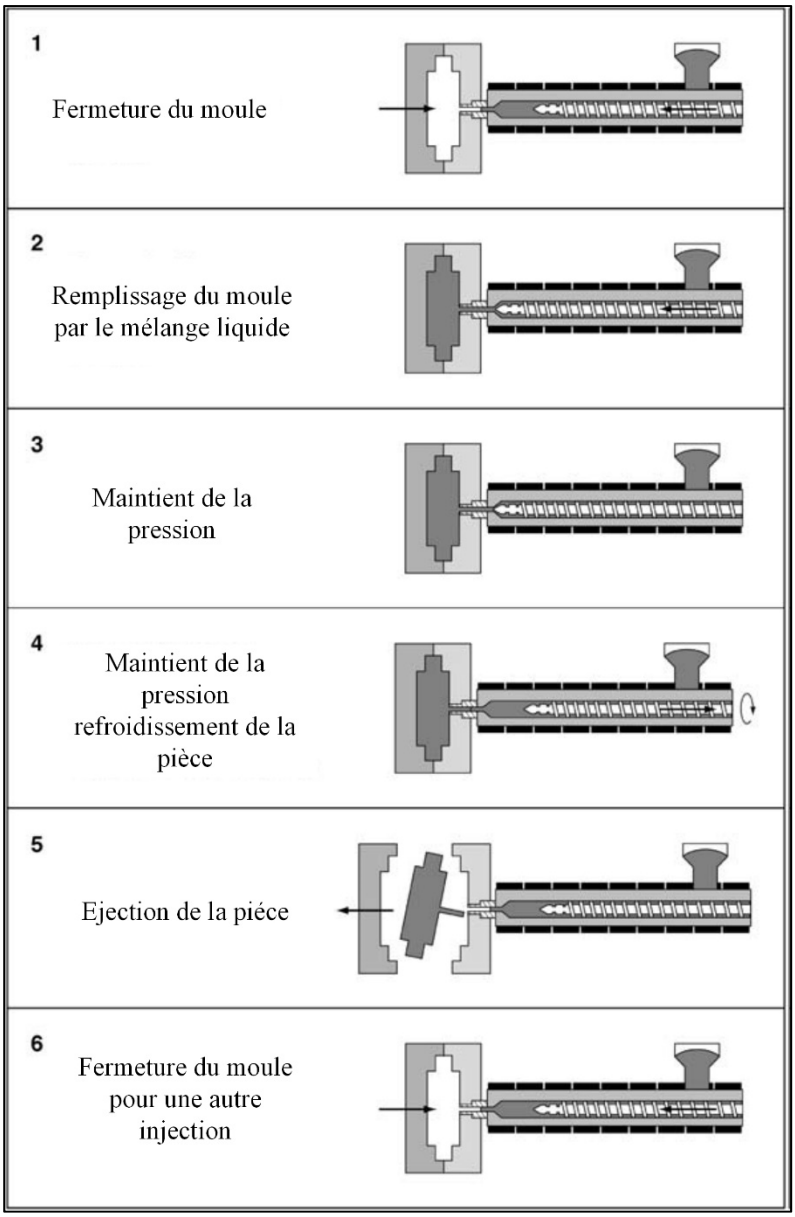

Figure 1.6 Aperçu du processus de moulage par injection.(Heaney, 2012)

1.1.1.3 Déliantage

Le déliantage permet de retirer le liant de la pièce à vert (Figure 1.2c). Tel que mentionné plus haut, les liants sont des composés organiques qui peuvent être retirés en utilisant différentes approches par l'utilisation de solvant, de chaleur ou une combinaison des deux pour créer une

réaction catalytique. C'est une étape très délicate à maîtriser afin d'éliminer le maximum du liant durant un temps faible sans créer de défaut sur la pièce (Itoh, Harikou, Satoh, & Miura, 2002). Il existe deux étapes de déliantage distinctes où la première étape consiste à ouvrir des orifices jusqu'à la surface de la pièce qui jouent le rôle des canaux pour retirer complètement le liant restant jusqu'au cœur de la pièce pendant la deuxième étape tel qu'illustré à la Figure 1.7. La pièce ainsi fabriquée est appelés pièce brun (ou en anglais *brown part*).

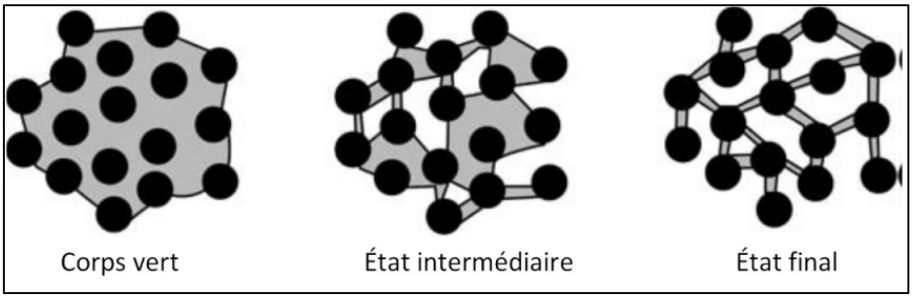

Figure 1.7 Schéma du déliantage (Enneti, 2005)

1.1.1.4 Frittage

Le but ultime du procédé MIM est d'obtenir une pièce métallique possédant une complexité de forme comparable à celle obtenue par la fonderie en utilisant les poudres tout en maintenant la forme de pièce injectée et déliantée (Figure 1.2d). Cette étape finale de consolidation de la poudre se nomme le frittage où la pièce déliantée est soumise à une température élevée (légèrement inférieure à la température de fusion) sous une atmosphère protectrice ou réactive. L'objectif de cette étape est d'éliminer la majorité des porosités qui occupaient la place du liant enlevé lors du déliantage. Le rétrécissement de la pièce brun doit être isotropique pour conserver la géométrie initiale et surtout éviter l'apparition de défauts. La Figure 1.8 présente une pièce avant et après le frittage où on voit bien le rétrécissement important de la pièce après le traitement de frittage (Song, Gelin, Barrière, & Liu, 2006).

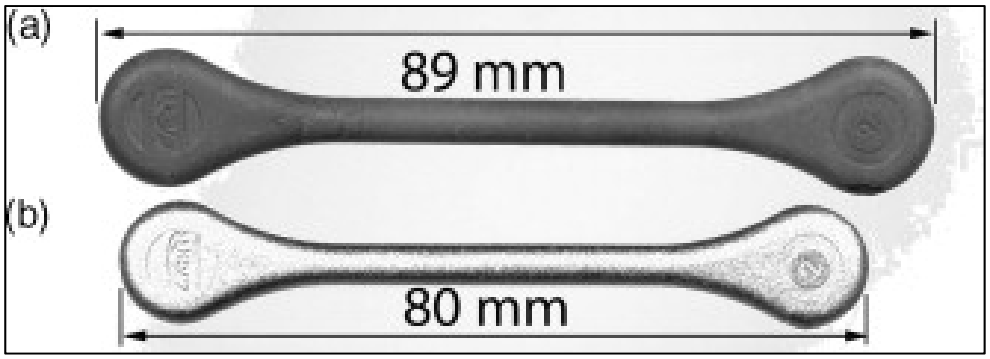

Figure 1.8 (a) pièce déliantée (avant frittage) et (b) pièce après frittage (Obasi, Ferri, Ebel, & Bormann, 2010)

Le frittage est une étape clé du procédé MIM permettant de contrôler le retrait de la pièce et obtenir un taux de porosité acceptable. La pièce finale possède généralement une résistance mécanique proche des matériaux forgés (ex. : 90 % de la résistance mécanique) qui est gérée par le taux de porosités et le développement d'une microstructure adéquate composée de grain et de joints de grains avec une densité généralement comprise entre 95 et 98 % de la densité théorique du matériau. Finalement, certains post traitements au frittage peuvent être effectués pour améliorer les performances ou l'apparence de la pièce par l'utilisation du grenaillage, du pressage isostatique à chaud (ou en anglais *hot isostatic pressing, HIP*) et le polissage tel qu'illustré à la Figure 1.9.

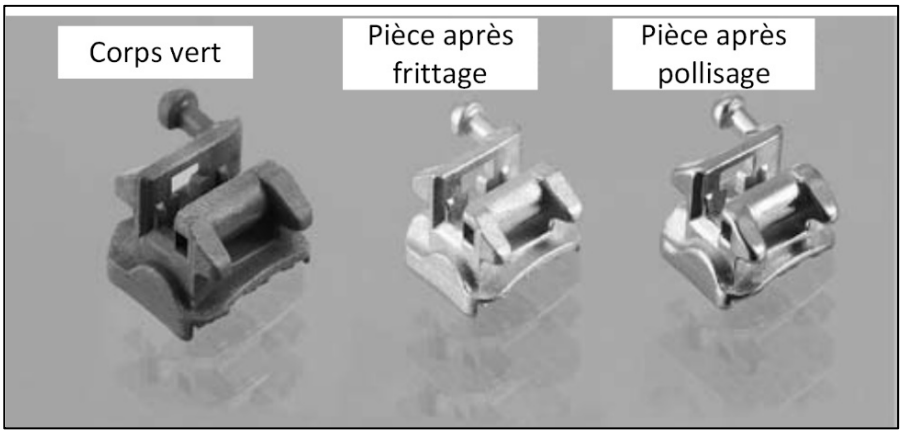

Figure 1.9 Pièce après frittage et polissage (Heaney, 2012)

1.1.2 Avantages du procédé MIM

Les principaux avantages de l'injection des poudres métallique MIM sont la complexité géométrique élevée (Figure 1.10), le faible coût de production, l'applicabilité à une large gamme d'alliage métallique, les tolérances géométriques élevées et les propriétés finales élevées des pièces. Les produits provenant du MIM sont donc compétitif avec la plupart des autres procédés de fabrication conventionnelle et particulièrement avec la coulée sous pression (fonderie) tel que présentée au Tableau 1.1.

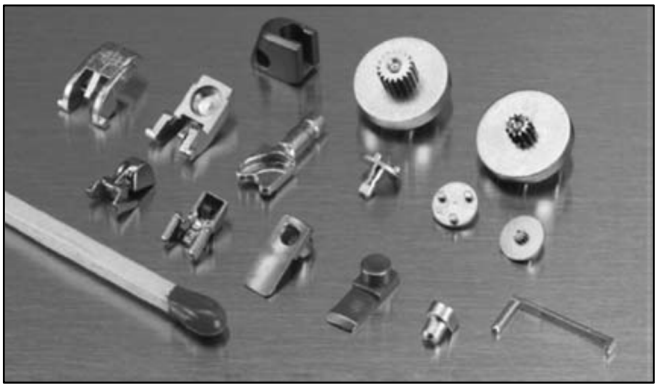

Figure 1.10 Engrenages et autres pièces de montre
(PARMACO AG, Switzerland)

Tableau 1.1 Comparaison des qualités des pièces
(http://www.technocampus.be/fad/pristipim/documents/formationPRESENTIELLE-GENERALITES-indus.pdf)

Paramètres	*MIM*	Usinage	Fonderie	Estampage	Compactage-Frittage
Densité	95 %	100 %	98 %	100 %	85-90 %
Résistance à la traction	Haute	Haute	Haute	Haute	Basse
État de surface	Bon	Bon	Moyen	Bon	Moyen
Rapport dimension/poids	Bon	Moyen	Moyen	Bon	Moyen
Complexité des pièces	Haute	Haute	Moyenne	Basse	Basse
Possibilité de réaliser des parois minces	Élevée	Basse	Élevée	Élevée	Élevée

1.1.3 Injection des poudres métalliques à basse pression (LPIM)

L'injection des poudres métallique à basse pression (ou en anglais *low-pressure powder injection molding, LPIM*) présente quelques différences par rapport au procédé MIM conventionnel où ce dernier utilise une haute pression pouvant aller jusqu'à 200 MPa. En effet, la pression d'injection utilisée en LPIM ne dépasse généralement pas 1 MPa. Ce jeune procédé se distingue surtout par rapport à ces mélanges à faible viscosité inférieure à 10 Pa·s et par des températures d'injection très faible inférieure à 120°C (Fareh, Demers, Demarquette, Turenne, & Scalzo, 2016; Sardarian, Mirzaee, & Habibolahzadeh, 2017). Le procédé LPIM était initialement utilisé pour les poudres de céramique et est devenue rapidement intéressant pour le développement de pièce métallique à haute valeur ajoutée surtout dans le domaine de l'aéronautique et l'industrie médicale. Les avantages du procédé LPIM par rapport à la technologie conventionnelle incluent une moulabilité très importante grâce à la basse viscosité des mélanges ce qui permet de concevoir des pièces plus complexes, des moules significativement moins dispendieux dû aux faibles pressions d'injection et un coût d'opération du procédé plus bas par l'utilisation de pression d'air ou de piston à faibles forces (Costa, Michels, & Kipper, 2018; Gholami & Demers).

1.2 Simulation numérique de la phase d'injection

Cette section présente les principaux résultats de simulation numériques de la phase d'injection du procédé MIM et LPIM reportés dans la littérature.

1.2.1 Comparaison des logiciels disponibles dans la littérature

Plusieurs logiciels sont capables de simuler l'injection bien qu'il existe certaines différences entre eux. Le Tableau 1.2 résume les logiciels trouvés dans la littérature par l'étudiant à la maitrise Vincent Raymond (Raymond, 2012). Les limitations et les forces de chaque logiciel présenté dans le Tableau 1.2 sont discutées en détails dans sa thèse.Il affirme que ProCAST a bien prédit les modèles de remplissage et l'emplacement de la ligne de soudure. Pourtant, la pressions et les températures calculées dans la cavité ne correspondaient pas aux données

expérimentales. Aussi, Plasview3D qui est le programme interne de simulation de l'injection plastique au Centre national de recherche et Conseil-industreil Institut des matériaux (NRC-IMI). Ce logiciel est un logiciel solveur tridimensionnel pour un écoulement de fluide parallèle utilisant la méthode des éléments finis. Le code a été écrit à l'origine pour l'injection plastique 3D,mais par la suite été utilisé pour le MIM.

Tableau 1.2 Logiciels d'injection dans la littérature (Raymond, 2012)

Logiciel	Domaine	Pays de développement
ANSYS (Fluent, CFX, other)	3D	Canada
Moldex3D	3D	USA
Moldflow Synergy	3D	Canada
PIMSolver	2.5D	South Korea
Plasview3D	3D	Canada
Pohang University	3D	South Korea
ProCAST	3D	USA
Sigmasoft	n/d	USA
FEAPIM	3D	France

Binet et al. (Binet, 2005) ont réalisé une étude expérimentale et numérique de l'injection d'un produit réel réalisé avec l'injection du mélange à base d'acier inoxydable AISI 316 pour le MIM haute pression. Cette étude repose sur le calcul par éléments finis à l'aide d'un logiciel commercial non mentionné par les auteurs. La propagation de la matière à l'intérieur de la cavité du moule pour différents temps d'injection est montrée à la Figure 1.11 et ces résultats ont été validés par des expériences.

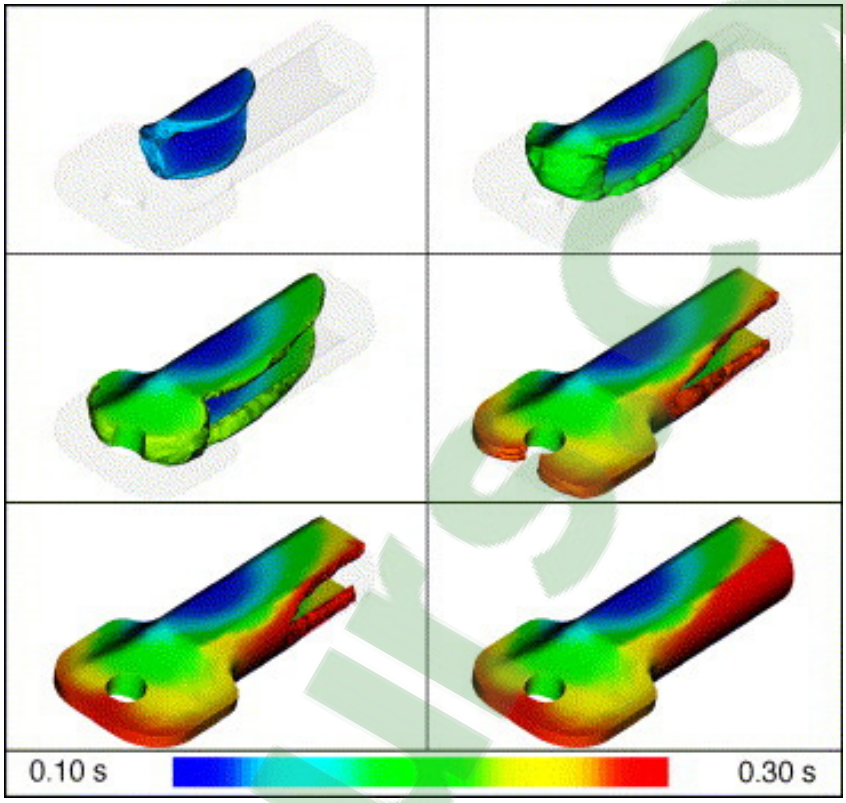

Figure 1.11 Simulation de la phase d'injection (Binet, 2005)

Yin et al. (Yin, Wang, Qu, Jia, & Johnson, 2011) ont utilisé ANSYS CFX comme logiciel de calcul par éléments finis en s'appuyant sur un modèle fluide biphasé mais en négligeant l'interaction entre le mélange et l'air. Ils ont montré que le modèle était capable de prédire la phase de remplissage de l'empreinte et les zones de faible concentration de poudre. Ils ont été en mesure de traiter le problème de la ségrégation de la poudre en se basant sur le mélange biphasé (Figure 1.12)

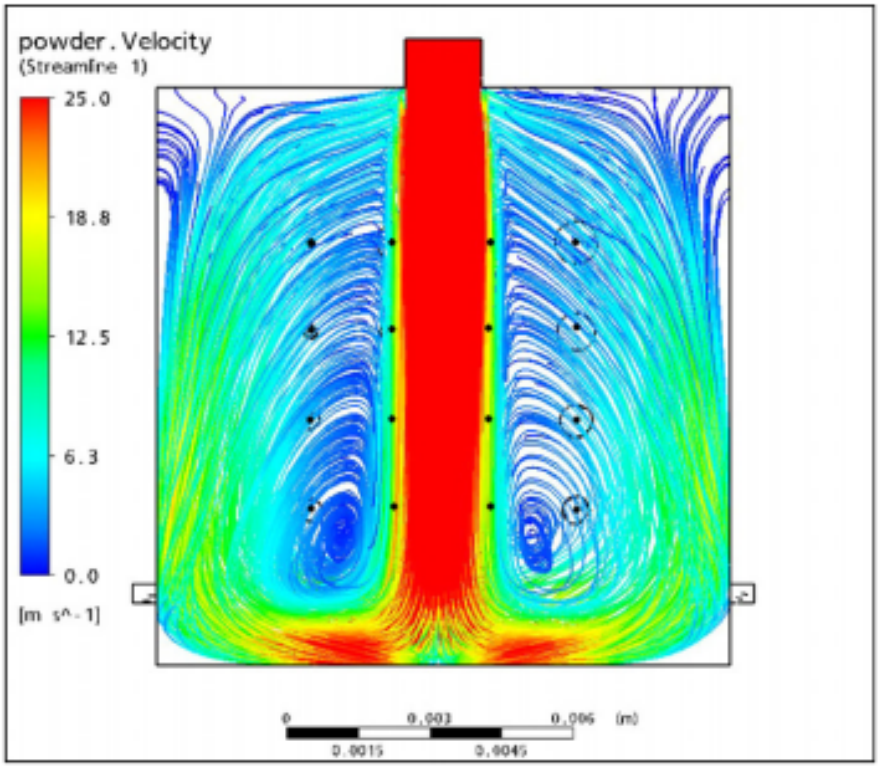

Figure 1.12 Détection de la vitesse des particules de la poudre
(Yin et al., 2011)

La simulation numérique de la phase d'injection est une étape essentielle pour la compréhension et la résolution des problèmes rencontrés lors de la production. L'évolution de la simulation numérique au niveau du domaine d'injection des poudres a marqué une progression importante avec Modflow Synergy qui contient un module pour l'injection des poudres. La simulation de l'injection des poudres métalliques MIM est relativement complexe à cause de l'écoulement 3D d'un fluide composé d'un liant et des particules de poudre (fluide non-Newtonien) en fonction des échanges thermiques à la Figure 1.13 présente l'architecture de la simulation en fonction des entrées, les étapes à suivre avec Moldflow Synergy 2019.

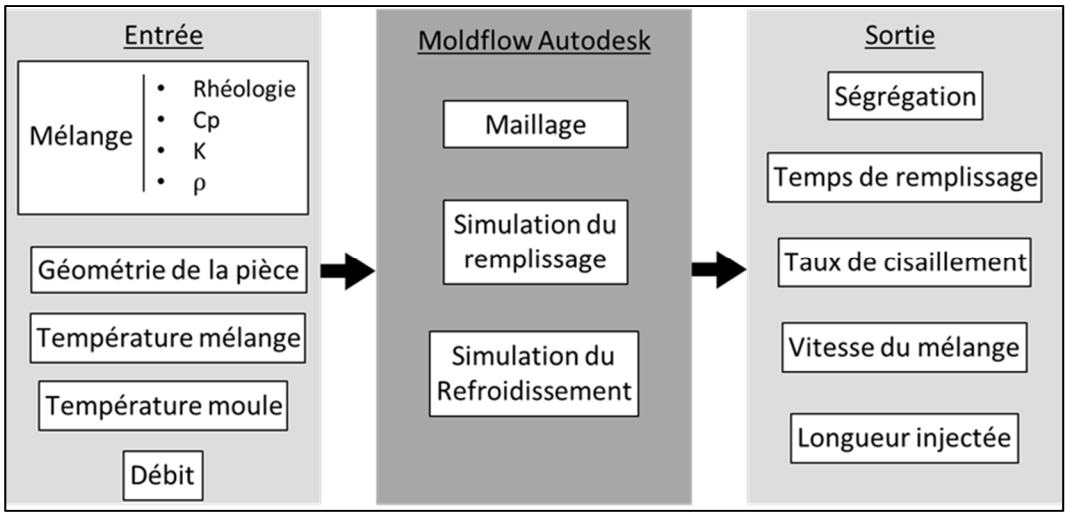

Figure 1.13 Architecture de la simulation numérique avec Autodesk Moldflow Synergy

Bien que l'application Moldflow ait été développée pour l'injection des plastiques, ce logiciel peut aussi être utilisé afin de simuler l'injection du procédé MIM en modifiant simplement les propriétés des mélanges injectés. La simulation du MIM nécessite l'attribution d'une géométrie, l'établissement des propriétés du mélange à injecter et la définition des conditions initiales et des conditions aux limites. La matière première est alors virtuellement injectée à l'état liquide et se solidifie dans la cavité du moule. Pour la simulation de cette étape, il est donc nécessaire d'obtenir les propriétés rhéologiques du mélange à l'état fondu, les propriétés thermique et la densité de la matière première tel qu'illustré à la Figure 1.13. Les conditions initiales sont le débit d'injection (ou la pression), la température du moule et la température de la matière. À partir d'ici et pour le reste de la revue de la littérature, seulement Moldflow Synergy sera discuté. Le choix de Moldflow Synergy 2019 est basé sur le succès des résultats reportés dans la littérature. Plusieurs chercheurs ont simulé l'injection des poudres métallique MIM à haute pression (mélanges métallique et céramique) et à basse pression (mélanges céramique seulement) avec Moldflow et ils ont obtenues des résultats proches des résultats expérimentaux. Le module de concentration de poudre utilise le modèle d'équilibre de suspension SBM (*Suspension balance model* en anglais) pour prédire l'effet de ségrégation de la poudre.

1.2.2 Méthode de résolution numérique avec Moldflow

La simulation numérique de la phase d'injection du mélange poudre-liant avec Moldflow est basée sur le modèle d'équilibre de phases liquide et solide pour la prédiction de l'effet de la ségrégation des poudres dans le mélange liquide. En conséquence, la ségrégation des poudres est induite par le taux de cisaillement. Le modèle d'équilibre de phases modélise le fluide et les particules métalliques en deux phases, mais les équations complètes de Navier-Stokes ne sont résolues que sur le mélange sous la forme d'un fluide. La résolution des équations est faite par la méthode des éléments finis. Dans Moldflow, le modèle SBM est défini par les équations suivantes qui décrivent dans l'ordre la conservation de masse du fluide, la conservation du moment, la conservation d'énergie et l'équilibre de masse des particules.

$$\frac{\delta\rho}{\delta t} + \nabla \cdot (\rho \vec{V}) = 0 \tag{1.1}$$

$$\rho \frac{D\vec{V}}{Dt} = -\nabla P + \nabla \cdot \vec{\vec{\tau}} + \rho \vec{g} \tag{1.2}$$

$$\rho C_p \frac{DT}{Dt} = \nabla \cdot (K \nabla T) + \vec{\vec{\tau}} : \nabla \vec{V} + \beta T \frac{DP}{Dt} \tag{1.3}$$

Avec β l'expansivité donnée par *:*

$$\beta = -\frac{1}{\rho}\frac{\partial\rho}{\partial T} \tag{1.4}$$

$$\frac{\partial\phi}{\partial t} + V \cdot \nabla = -\nabla \cdot j_{\perp} \tag{1.5}$$

où ρ est la masse volumique du liant, t est le temps, $\vec{V}$ est le vecteur de vitesse, $\vec{\vec{\tau}}$ est le tenseur de contrainte visqueuse, P est la pression, $\vec{g}$est l'accélération gravitationnelle, k est la conductivité thermique, C_p est la capacité thermique, ϕ est la fraction volumique de poudre et $j_{\perp}$ est le flux de particules de poudre donnée par :

$$j_{\perp} = \frac{2a^2}{9\eta_0} f(\phi) \nabla \cdot \Sigma_p \tag{1.6}$$

Où *f(ϕ)* est la fonction de sédimentation, η_0 est la viscosité du liant, *a* est le diamètre des particules et Σ_p est la contrainte normale de particule donnée par :

$$\Sigma_p = -\eta_0 \eta_n \dot{\gamma} Q \tag{1.7}$$

Où η_n est la contrainte normale de viscosité et $\dot{\gamma}$ est le taux de cisaillement donné tous deux par :

$$\eta_0 = k_n \left(\frac{\phi}{\phi_m}\right)^2 \left(1 - \frac{\phi}{\phi_m}\right)^{-2} \tag{1.8}$$

$$\dot{\gamma} = \sqrt[2]{2E : E} \tag{1.9}$$

Où ϕ_m est le chargement solide maximale, k_n est la conductivité thermique de la poudre, *Q* est le tenseur d'anisotropie de contrainte normale donné par :

$$Q = \begin{bmatrix} \lambda_1 & 0 & 0 \\ 0 & \lambda_2 & 0 \\ 0 & 0 & \lambda_3 \end{bmatrix} \tag{1.10}$$

Où les λ_i sont les contraintes normales suivant la direction d'écoulement, sa perpendiculaire et la rotation. La simulation nécessite généralement un modèle avec un maillage 3D afin de résoudre tout le système des équations précédentes. La simulation de l'injection est basée sur les principes de la dynamique des fluides numérique (ou anglais *computational fluid dynamic, CFD*) en fonction de toutes les équations précédentes. Sadarian a étudié le comportement des mélanges à basse viscosité LPIM à base de poudre céramique. Dans une de ces études, il a fait l'objet d'une étude approfondie des paramètres de moulage, l'effet de la température et de la pression d'injection sur les propriétés d'un mélange à base d'alumine dans le procédé LPIM (Sardarian, 2017).

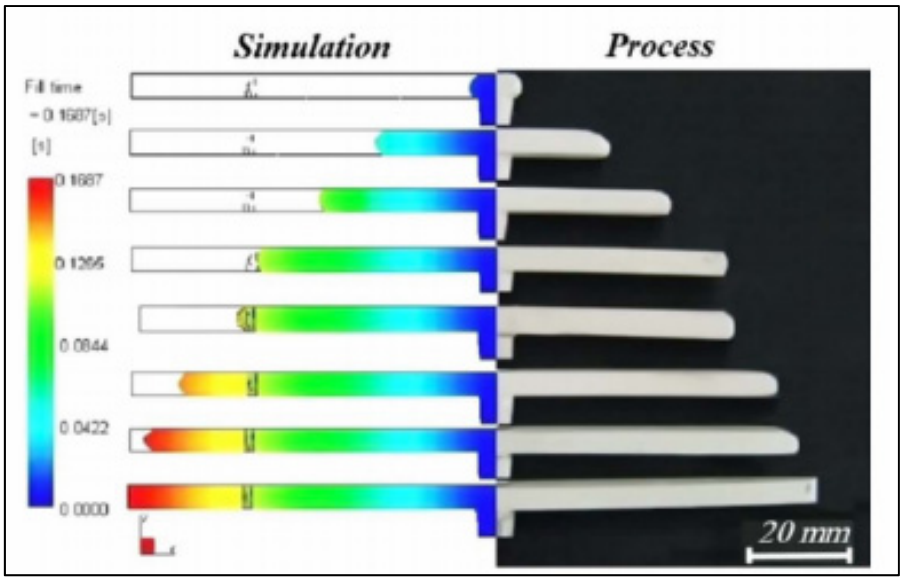

Figure 1.14 : comparaison entre les résultats de la simulation et l'expérimentale le front de matiére lors de l'injection (Sardarian, 2017)

Aussi, il a inspecté l'étape de remplissage du moule par injection à basse pression (LPIM) d'alumine qui a été simulée avec la méthode des éléments finis avec Moldflow Autodesk (Figure 1.14). La forme du front de fusion obtenue à partir de la simulation correspondait bien aux expériences La comparaison entre ces résultats de simulation et ces résultats expérimentaux a montré un bon accord en ce qui concerne l'avance des fronts de fusion (Sardarian, 2017). Les résultats trouvés par Sardarian en LPIM pour les céramiques nous poussent à inspecter le comportement des mélanges à base des poudres métallique.

CHAPITRE 2

PROBLÉMATIQUE ET OBJECTIFS

Problématique : On se basant sur la revue de la littérature, il est bien connu que la qualité du produit final fabriqué par l'injection des poudres métallique à basse pression LPIM dépend de la qualité de la matière première (mélange poudre-liant) et des paramètres qui contrôlent les étapes d'injection, déliantage et frittage. Tel que mentionné au Chapitre 1, le procédé LPIM nécessite des mélanges à basse viscosité mais jusqu'à maintenant, les efforts ont été orientés principalement vers l'étude des mélanges à haute viscosité pour l'injection à haute pression HPIM. Ainsi, les données disponibles dans la littérature à propos de LPIM sont très limitées ou simplement absente car les mélanges métalliques à base de cire ont été principalement développé en circuit fermé en industrie. Par conséquent, **l'injection basse pression des poudres métalliques n'a jamais été simuler**, il existe seulement des travaux de recherche à propos de l'injection à basse pression des poudres céramiques. Plusieurs travaux de recherche se concentre sur développement orienté vers les équipements (presse, moule, cycles de frittage, etc.) mais pas vraiment les techniques de simulation qui a même créé un manque d'information sur les propriétés des mélanges LPIM.

Objectif : L'objectif principal du projet est de caractériser expérimentalement les mélanges et simuler numériquement la phase d'injection du moulage à basse pression des poudres métalliques. Spécifiquement, certaines propriétés du mélange comme **la viscosité, la chaleur spécifique, la densité et la conductivité thermique ont été caractérisées pour la simulation et pour quantifier l'impact de la forme et de la taille de la poudre sur le comportement des mélanges**. Par la suite, ces valeurs ont été implémentées dans le logiciel de simulation Autodesk Moldflow Synergy 2019 afin de prédire la longueur injectée, la vitesse frontale du coulé, le temps de remplissage, le taux de cisaillement et l'ampleur de la ségrégation des poudres. **Finalement, toutes ces métriques ont été validées expérimentalement sur des injections à l'échelle réelle**.

.

CHAPITRE 3

MÉTHODOLOGIE EXPÉRIMENTALE

Ce chapitre présente les équipements utilisés lors de la caractérisation des mélanges étudiés. **Les conditions expérimentales de toutes les techniques de mesure sont décrites en détail dans les deux articles scientifiques présentés aux Chapitres 4 et 5**. Afin d'éviter la répétition des informations décrivant la méthodologie, cette section ne présente que les informations supplémentaires qui n'apparaitraient pas dans les deux articles scientifiques.

3.1 Caractérisation des poudres sèches

La distribution de la taille des particules et de la surface spécifique des différents lots de poudres métalliques ont été mesurées en utilisant un analyseur de particules à diffraction laser LS 13 320 Beckman Coulter (Figure 3.1). L'objectif de cette analyse est de chercher la différence entre les poudres utilisées de point de vue taille de poudre (d_{10}, d_{50} et d_{90}) et aussi la surface spécifique des chaque lot de poudre qui est un paramètre très important à étudier.

Un microscope électronique à balayage (Hitachi 3600, Figure 3.1.b) a été utilisé pour évaluer qualitativement la forme des particules de chaque lot de poudre sèche et d'examiner l'état de la matières premières après la préparation du mélange avec un détecteur d'électrons secondaires pour les poudres sèches et un détecteur d'électrons rétrodiffusés sous pression partielle pour les mélanges poudre-cire.

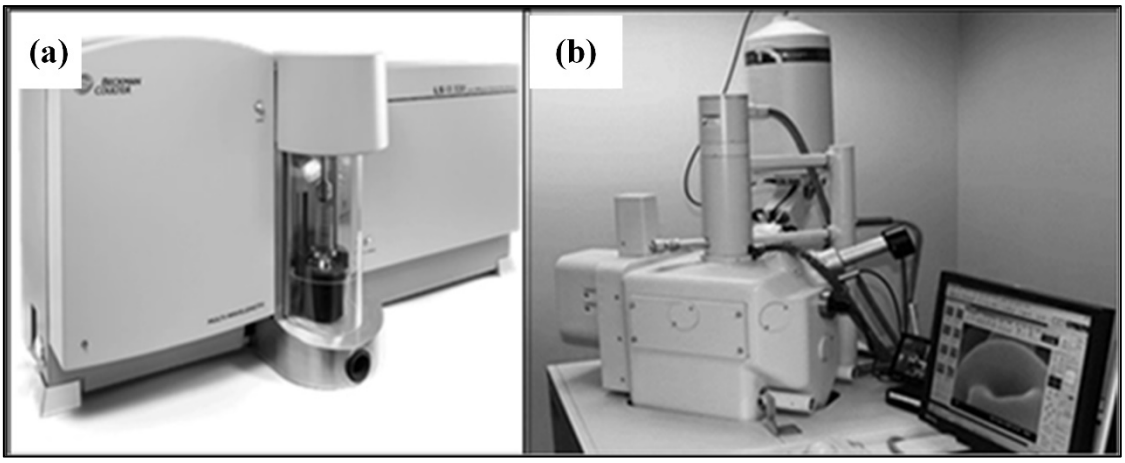

Figure 3.1 Caractérisation des poudres sèches (a) analyseur de taille des particules et (b) microscope électronique à balayage (Hitachi 3600)

3.2 Caractérisation rhéologique

L'analyse rhéologique permet de quantifier la résistance (ou la facilité) de l'écoulement de la matière fluide sous l'effet d'une contrainte appliquée. L'un des principaux paramètres rhéologiques est la viscosité qui est, pour un mélange de poudre et de liant, dépendant du taux de déformation en cisaillement et de la température. Le comportement rhéologique des mélanges poudre-cire a été caractérisé en utilisant un rhéomètre rotationnel Anton Paar MCR 302 avec un cylindre concentrique CC-17 et un système de mesure à température contrôlée C-PTD 200 Peltier (Figure 3.2).

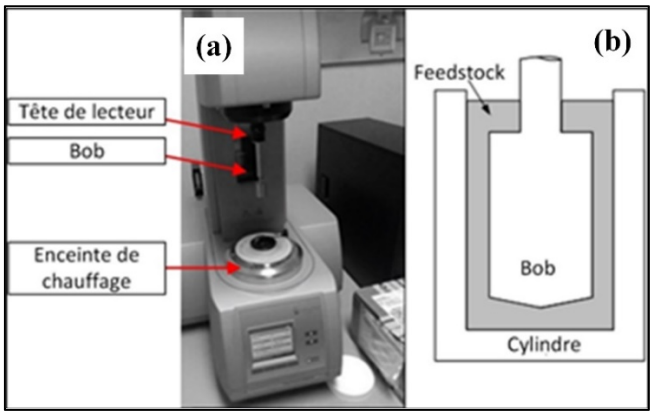

Figure 3.2 (a) Rhéomètre et (b) instruments utilisés

3.3 Caractérisation thermique

La calorimétrie différentielle à balayage (ou en anglais *Differential scanning calorimetry,* DSC) est une technique d'analyse thermique des matériaux. La chaleur spécifique et les températures de fusion ont été obtenues avec cette technique en utilisant un PerkinElmer Pyris 1 (Figure 3.3a). La conductivité thermique est une propriété très importante pour la simulation de la phase de l'injection afin de calculer les échanges thermiques lors de l'injection et durant le refroidissement. Les essais ont été effectués avec un appareil de flash laser LFA 447 Nano Flash (Figure 3.3b). En date de la soumission de ce document, les essais sont toujours en cours à l'Université de Dalhousie. Ainsi, pour être capable d'alimenter la simulation numérique, le modèle de Maxwell a été utilisé pour calculer la conductivité thermique théorique à l'état solide et liquide en fonction des conductivités thermiques des matériaux utilisés pour le mélange étudié (Tableau 3.1) en utilisant l'équation (5.4) présentée plus loin dans l'article #2.

Tableau 3.1 Conductivités thermiques des constituants du mélange

T		CW		PW		EVA		Poudre 17-4PH	
T(K)	k(W/mK)	T(K)	k(W/mK)	T(K)	k(W/mK)	T(K)	k(W/mK)	T(K)	k(W/mK)
298	0,41	298	0,1456			298	0,34	298	17,9
308	0,39	308	0,1456	307	0,346	308	0,34	308	17,9
318	0,38	318	0,1456	321	0,339	318	0,34	318	17,9
328	0,37	328	0,1456			328	0,34	328	17,9
338	0,36	338	0,1456	336	0,167	338	0,34	338	17,9

Pour étudier l'homogénéité des mélanges, le pourcentage volumique de poudre a été quantifié en utilisant un analyseur thermogravimétrique (TGA) PerkinElmer Diamond TG / DTA (Figure 3.3c). Cet appareil permet de créer un balayage en température et de bruler les polymères et d'obtenir au final, la masse de la poudre sèche qui était présente dans mélange donné.

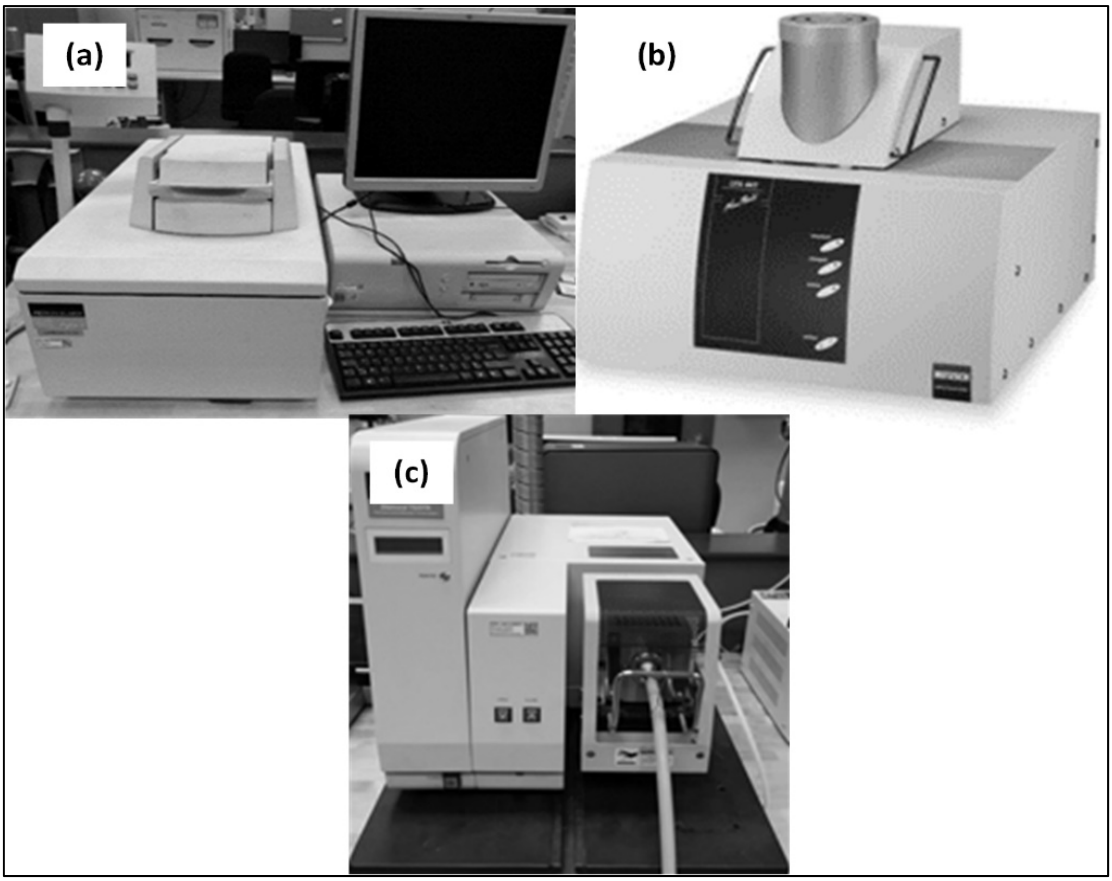

Figure 3.3 (a) Calorimètre différentiel à balayage, (b) Flash laser et (c) Analyseur thermogravimétrique (TGA)

3.4 Densité

La densité du mélange qui présente la masse du mélange par rapport à son volume a été obtenue avec le dispositif de détermination de la masse volumique Sartorius YDK03 (Figure 3.4) en utilisant la méthode d'Archimède. Cette méthode consiste à prendre la masse à sec et la masse mouillé et de calculer la densité à partir de l'équation 5.7 présentée plus loin.

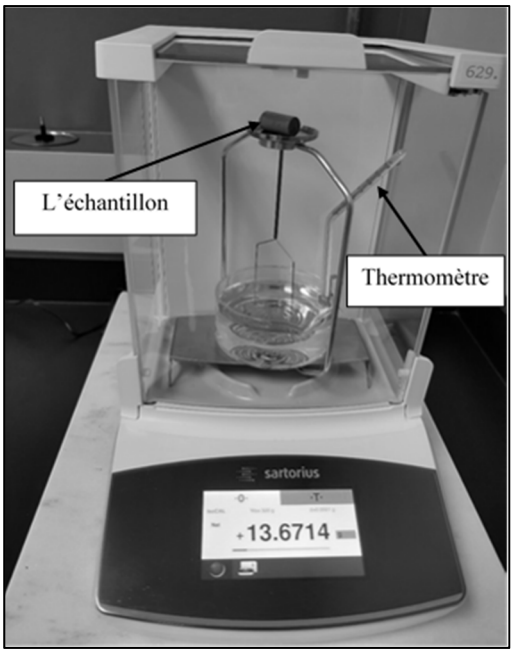

Figure 3.4 Dispositif Sartorius de détermination de la densité

3.5 Tests d'injections

Les injections ont été effectuées à l'aide d'une presse d'injection de laboratoire (Figure 3.5) dans laquelle un nouveau concept d'injection a été développé pour minimiser la ségrégation des mélanges à faible viscosité et pour mettre en valeur le procédé d'injection des poudres métalliques à basse pression LPIM. Le traitement vidéo durant l'injection est effectué par les logiciels suivants, Virtual Dub, pour enregistrer le film avec le nombre image souhaitée par seconde (fps), Avimeca pour indiquer et saisir les coordonnées du front d'écoulement et Regressi pour traitement donné afin de chercher la vitesse d'injection.

La Figure 3.5 présente une presse d'injection à basse pression développée au sein du laboratoire MIM de l'École de technologie supérieure. Cette presse est munie d'une table glissante qui permet d'éliminer le canal d'injection permanent et de pouvoir injecter des mélanges à très faible viscosité où ce système est à l'étape de l'application de brevet international.

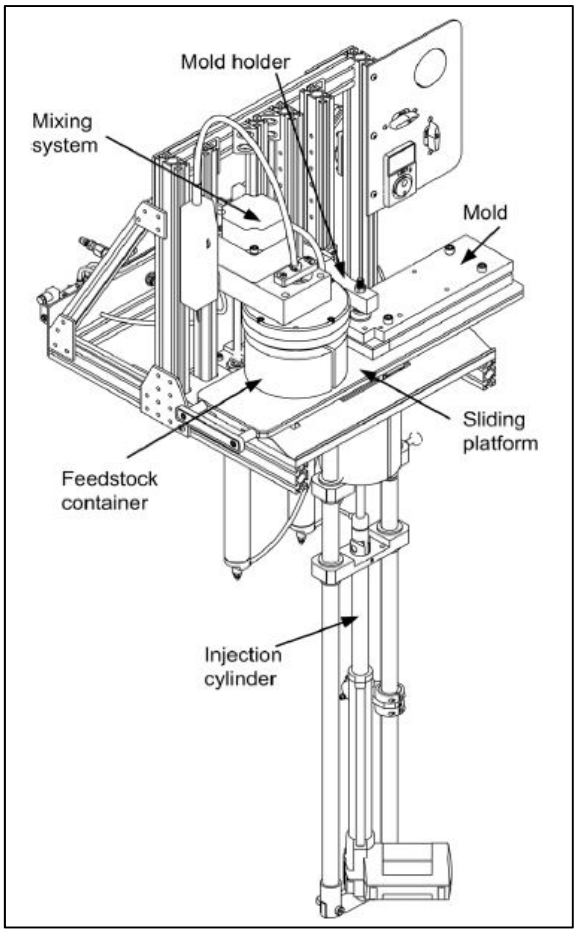

Figure 3.5 Presse d'injection à basse pression
(Lamarre,Demers, & Chatelain, 2017)

3.6 Avant-propos chapitre 4 et chapitre 5

Le chapitre 4 présente l'article 1 qui a été soumis dans « Journal of Materials Engineering and Performance » édité par Springer. L'objectif de cet article est d'étudier l'effet de la forme et la

taille des particules de la poudre métallique (17-4PH) sur les propriétés rhéologiques, thermiques et de ségrégation des mélanges pour l'injection à basse pression. Le meilleur mélange trouvé dans le chapitre 4 est utilisé dans le chapitre 5 pour les simulations et les tests d'injections réelles pour l'étude de la phase d'injection à basse pression et pour la vérification de la capacité du logiciel de simuler la ségrégation des poudres lors de l'injection. Ma contribution dans cet article a été d'effectuer tous les essais expérimentaux et d'écrire entièrement l'article proprement dit. Les deux autres coauteurs de cet article sont mon directeur et codirecteur qui m'ont supervisé tout au long des différentes phases du projet incluant la de rédaction de l'article.

Le chapitre 5 présente l'article 2 qui a été soumis dans « Journal of Materials and Design » édité par Elsevier. L'objectif de cet article est de de simuler le comportement de remplissage du moule lors de l'injection par le mélange à base de poudre métallique. La caractérisation a été réalisée avec un mélange formulé à partir d'une poudre d'acier inoxydable 17-4PH à 60 vol. %. La comparaison des résultats de entre la simulation et les tests d'injection réels montre une bonne similitude. La solution Moldflow Synergy 2019 (Autodesk) a été validée avec succès par des expériences. Ma contribution dans cet article a été d'effectuer la majorité des essais expérimentaux, de réaliser toutes les simulations numériques et d'écrire entièrement l'article. Le coauteur Raphaël Côté m'a supporté dans la réalisation de plusieurs essais d'injection et l'obtention des valeurs du modèle de Cross-WLF. Le coauteur Mehran Sardarian est un expert dans le domaine de la simulation numérique de l'injection des poudres céramique à basse pression et il construit un modèle Matlab capable de calculer les paramètres de Cross-WLF en plus de me conseiller sur la résolution de problèmes de la simulation numérique en utilisant Autodesk Moldflow Synergy 2019. Finalement, les deux autres coauteurs de cet article sont mon directeur et codirecteur qui m'ont supervisé tout au long des différentes phases du projet incluant la rédaction de l'article

CHAPITRE 4

ARTICLE #1: EFFECT OF POWDER SHAPE AND SIZE ON RHEOLOGICAL, THERMAL, AND SEGREGATION PROPERTIES OF LOW-PRESSURE POWDER INJECTION MOLDING FEEDSTOCKS

Mohamed Aziz Ben Trad [1], Vincent Demers[1*] , Louis Dufresne[1]

[1] École de technologie supérieure, 1100 Notre-Dame West, Montreal, QC, H3C 1K3, Canada

Article soumis pour publication, septembre 2018

4.1 Abstract

Optimization of molding parameters at different filling stages requires that the characteristics of low-viscosity feedstocks must be well known. In this study, the influence of the particle size (3, 7, and 12 μm) and powder morphology (gas- and water atomized) were quantified using different feedstock formulations based on 17-4 PH stainless steel powder combined with the same binder system. The specific heat capacity, viscosity, and segregation level were assessed using a differential scanning calorimeter, a rotational rheometer, and a thermogravimetric analyzer. It was demonstrated that the feedstock prepared with gas-atomized powder exhibits a higher specific heat capacity value as compared to water-atomized powder. It was also shown that the viscosity profiles of feedstocks and the intensity of segregation depend significantly on the powder shape and size used in the feedstock formulation. For short processing times (e.g., < 1 min spent in molten state), a feedstock formulated with coarse gas-atomized powder can be considered as the best candidate for the injection process because its viscosity and segregation potential are relatively low. In this respect, the moldability index was used to predict that coarser water-atomized powder (i.e., 12 vs. 7 μm) will not have a significant effect on the molding properties, and can be seen as a potential means of decreasing shrinkage during sintering without impacting the injection properties. For very long processing times, the magnitude of segregation remains insignificant for feedstock formulated with fine powder. However, this important gain (i.e., no segregation) comes with a significant increase in viscosity, resulting in a decrease in the molding properties.

Keywords: Low-pressure powder injection molding, feedstock, rheology, specific heat capacity, segregation, 17-4PH

4.2 Introduction

Metal injection molding is a well-adapted process for the manufacture of small, precise, and complex shape metallic parts with high service properties and produced at low cost. The MIM process involves feedstock preparation by mixing a metallic powder with a molten binder, which is injected into a mold cavity to form the required shape after solidification of the binder. This green part is then debound and sintered to completely remove the binder and obtain a near-net shape dense metallic component (German & Bose, 1997; Hausnerova, 2011; D. Heaney, 2012). Recently, the high-viscosity feedstocks used in the conventional high-pressure powder injection molding process (HPIM, using an injection pressure varying from 50 to 200 MPa) have been modified to design new low viscosity feedstocks adapted for the low-pressure powder injection molding process (LPIM). These wax-based feedstocks are generally characterized by a low melting point (e.g., < 120°C) and low viscosity (e.g., < 10 Pa·s), leading to injections performed at pressures generally lower than 1 MPa (Hausnerova et al., 2017; Sardarian et al., 2017). Initially developed for the production of ceramic components, the LPIM process has been adapted for the fabrication of metallic parts in the aerospace and medical industries (Aslam et al., 2016; Ibrahim et al., 2012). The rheological behavior of the feedstock is a key parameter used to control the mold filling operation during injection. Mangel et al. were the pioneers in this regard, and used the spiral flow distance to demonstrate that the moldability of LPIM feedstocks is inversely proportional to its viscosity (Mangels & Williams, 1983). It is well known that powder characteristics influence the flow behavior of feedstocks. In general, the viscosity decreases with an increase in the particle sphericity, an increase in particle size, and a decrease in particle surface roughness (Contreras, Jimenez-Morales, & Torralba, 2010; Heaney, Zauner, Binet, Cowan, & Piemme, 2004; Jamaludin et al., 2010). Water and gas atomization are two techniques that are widely used to produce irregular and spherical particles that are utilized in HPIM and LPIM metallic-based feedstocks. It is generally well accepted that feedstocks formulated from a gas-atomized powder provide a better injection molding capability, but are generally more expensive than those formulated

from water-atomized powder. This moldability improvement is generally related to a decrease in interparticle friction combined with a decrease in energy required for the powder orientation with the flow during an injection. For LPIM feedstocks, the effect of the powder shape and size on the rheological behavior has mainly been studied for ceramic-based powder-binder mixtures (Hausnerová, Kitano, & Sáha, 2010; Schlechtriemen, Knitter, Haußelt, & Binder, 2013). The thermal properties of feedstocks are also crucial in setting the injection parameters and establishing the constitutive equations required to numerically simulate the injection step. Calorimetric analysis is routinely used in HPIM and in LPIM to measure the melting point of feedstock. This test is well-adapted to study the interaction between the binder constituents and to properly set the minimum injection temperature (Demers, Turenne, & Scalzo, 2015; Hausnerová, Kasparkova, & Hnátková, 2016; Standring, Blackburn, & Wilson, 2016; Zaky & Mohamed, 2010). This technique is also somewhat used in HPIM to evaluate the specific heat capacity of different powder-binder mixtures and predict the solidification behavior during cooling of the component (Binet, Heaney, Spina, & Tricarico, 2005). The heat capacity of a given feedstock can easily be approximated by a rule of mixture using the heat capacities and weight fractions of each constituent (Chung, Carpenter, Cao, Liu, & Rhee, 1990), but this technique has thus far only been validated for a few HPIM feedstocks (Ishida & Rimdusit, 1999; Jamaludin et al., 2010; Kate, Enneti, Park, German, & Atre, 2014; Kowalski & Duszczyk, 1999; Liu, Loh, Tor, & Khor, 2002). For LPIM mixtures, the effect of the powder shape and size on the specific heat capacity has received very little attention in the literature. Segregation is an undesirable effect which refers to a fluctuation in solid loading within the feedstock (i.e., before or after injection), and which must be minimized to prevent distortions, cracks, warping, and heterogeneous shrinkage during the sintering step of the process. This inhomogeneous distribution of powder particles in the feedstock is generated by an improper mixing method during feedstock preparation, high shear deformation rate gradients during the molding process, or by the gravity of feedstock that remains idle during the process dead times (Faoud Fareh, Demers, Turenne, & Scalzo, 2016; Ihle, Tamburrino, & Vivero, 2013; Martin Jenni, Schimmer, Zauner, Stampfl, & Morris, 2008; M Jenni, Zauner, & Stampfl, 2009). The segregation phenomenon occurring during the injection stage has been well-studied using different numerical approaches to investigate the role of injection parameters and predict the

segregation effect through an injected part (Fang, He, Zhang, Yang, & Qu, 2014; Gelin, Barriere, & Song, 2010; He, Li, Lou, Li, & Liu, 2016). Recent studies on the segregation effects of LPIM molded parts have focused mainly on the development of experimental techniques to investigate the role of injection parameters or feedstock attributes in segregation. Hausnerova et al. developed an experimental technique based on SEM/EDX to detect powder-binder separation (Hausnerová & Sanétrník, 2013; Hausnerová, Sanétrník, & Ponizil, 2013). Demers et al. used the TGA technique to measure a nonuniform distribution of powder particles through rectangular and wedge-shaped molded parts processed by LPIM (Demers, Fareh, Turenne, Demarquette, & Scalzo, 2018; Hausnerová & Sanétrník, 2013; Hausnerová et al., 2013). Poh et al. demonstrated the strength of this TGA technique in the development of ceramic-based LPIM mixtures (Poh, Della, Ying, Goh, & Li, 2018). Shivashankar et al. used a capillary rheometer to investigate the segregation of low and moderate viscosity mixtures, while Mukund et al. combined capillary rheology and density measurements to quantify the powder-binder separation in moderate pressure powder injection molding process feedstocks (Mukund, Hausnerová, & Shivashankar, 2015; Shivashankar, Enneti, Park, German, & Atre, 2013)]. During injection dead times, segregation generated by gravity may occur for feedstocks that remain idle (e.g., that are trapped in the injection press), producing a powder-binder mixture that could be inappropriate for further injections. This type of segregation has only been superficially examined in a conventional HPIM due to the inherently high viscosity of feedstocks, which prevents the occurrence of this phenomenon. For LPIM feedstocks, an experimental model was developed and recently refined to highlight that the segregation of unmixed feedstocks depends on the binder constituents and idle time (Demers, 2018). The aim of this study is to investigate the effect of the powder shape and size on the rheological behavior, thermal properties, and segregation of metal-based LPIM feedstocks.

4.3 Material and measurements

4.3.1 Powder characteristics and feedstock preparation

Four different powder lots were used in this study (Tableau 4.1Tableau 4.1). Three water-atomized stainless steel 17-4PH powders (Epson Atmix Corporation, Japan), with a typical

nearspherical or ligament shape and nominal particle sizes of 3, 7, and 12 µm (Figure 4.1a-c), and one gas-atomized stainless steel 17-4PH powder (Sandvik Osprey Ltd, United Kingdom), with a spherical shape and a nominal particle size of 12 µm (Figure 4.1.d), were used. This precipitation-hardening stainless steel is widely used in the aerospace, chemical, petrochemical, and many other sectors for its high strength and good corrosion resistance.

Tableau 4.1 17-4PH powder characteristics

Powder lot	Atomization technique	Density (g/cm^3)	d_{10} (µm)	d_{50} (µm)	d_{90} (µm)	Specific surface area (m^2/g)	Supplier
PF-3K	Water	7.8	1.2	2.7	5.4	0.30	Atmix
PF-13F	Water	7.8	2.3	7.0	20.3	0.10	Atmix
PF-20F	Water	7.8	3.4	11.8	31.3	0.08	Atmix
S17700	Gas	7.8	3.0	11.3	27.5	0.09	Osprey

Each powder lot presented in Tableau 4.1 was combined with molten binder (90°C) in a laboratory mixer and blended for 45 minutes under vacuum. The solid loading was set at 60 vol. % of powder to prepare four different feedstocks using the same low melting point binder system formulated from 30 vol. % of paraffin wax, 7 vol. % of Carnauba wax (CW), 2 vol. % of stearic acid (SA), and 1 vol. % of ethylene vinyl acetate (EVA).

Tableau 4.2 Volume fraction of powder and binder used for feedstock formulations

Feedstock formulation	Melting point (°C)	Vol. %							
		Powder				Binder			
		PF-3K	PF-13F	PF-20F	S17700	PW	CW	SA	EVA
3-W	77.5	60	--	--	--	30	7	2	1
7-W	77.5	--	60	--	--	30	7	2	1
12-W	77.5	--	--	60	--	30	7	2	1
12-G	77.5	--	--	--	60	30	7	2	1

These binder constituents were selected due to their extensive use in LPIM, to help with the part ejection after mold filling, to promote the surfactant effect enhancing chemical links between the powder and binder, and to produce the thickening effect needed to control the segregation of powder (Leverkoehne, Coronel-Hernandez, et al., 2001; Majewska-Glabus, Zhuang, Vetter, & Duszczyk, 1995b; Omar, 2001). Feedstock formulations presented in Tableau 4.2 are referenced by their nominal powder sizes (i.e., 3, 7, or 12 μm) and atomization techniques (i.e., W for water or G for gas). For example, the feedstock 3-W is a mixture containing 60 vol. % of 3 μm water-atomized powder with 30 vol. % of PW, 7 vol. % of CW, 2 vol. % of SA, and 1 vol. % of EVA.

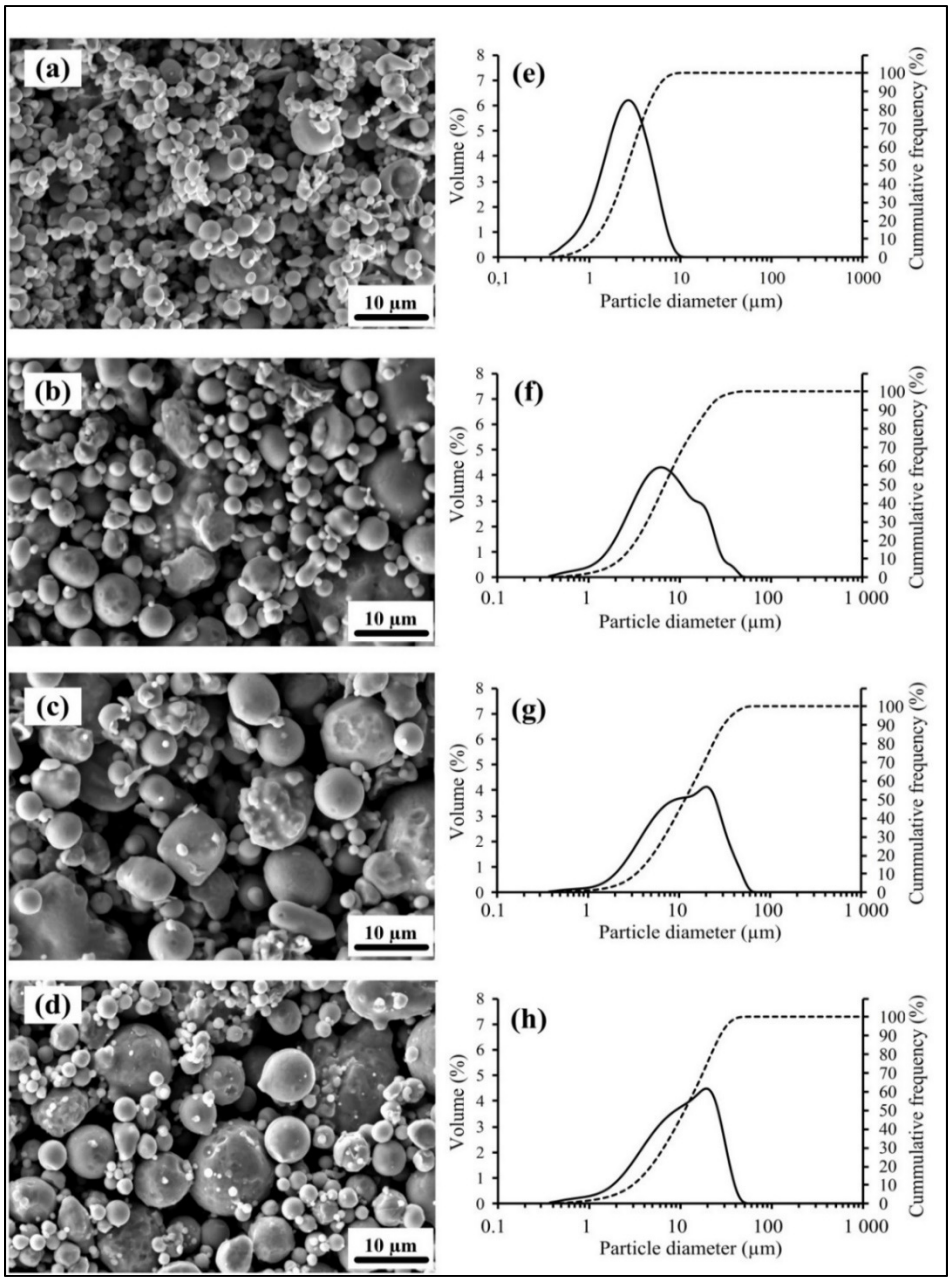

Figure 4.1 SEM photographs and particle size distribution of different 17-4PH stainless steel powder lots

4.3.2 Measurement

The particles' size distribution and specific surface areas were measured using an LS 13320 Beckman Coulter laser diffraction particle analyzer. Frequency curves and cumulative particle

size distributions were plotted in Figure 4.1e-h to assess the relative amount of particles constituting each powder lot and to quantify typical powder characteristics such as d10, d50, d90, and the specific surface area, all reported in Tableau 4.1. A scanning electron microscope (Hitachi 3600) was used to qualitatively evaluate the particle shape of each dry powder lot (Figure 4.1a-d) and to examine the segregated state of feedstocks (Figure 4.9) using a secondary electrons detector (under high vacuum) and a backscattered electrons detector (under partial pressure), respectively. Thermal properties were obtained with a PerkinElmer Pyris 1 differential scanning calorimeter (DSC). The melting point and specific heat of feedstocks were measured according to ASTM D3418 and ASTM E1269, respectively (ASTM-D3418, 2015; ASTM-E1269, 2018; Leverkoehne, Coronel-Hernandez, et al., 2001; Majewska-Glabus et al., 1995b; Omar, 2001). Feedstock and single-binder specimens with a mass ranging from 8 to 12 mg were encapsulated in standard aluminum hermetic pans and tested over temperatures ranging from 20 to 120 °C (heating rate of 10 °C·min^{-1}) under dry nitrogen gas flow (50 ml·min^{-1}). The DSC thermograms were recorded from the second heating cycle to minimize the thermal history and maximize the thermal contact between the pan and specimen. The melting points of each single binder are reported in Tableau 4.3.

Tableau 4.3 Melting points and density of the binders

Binders	Melting point (°C)	Density (g/cm^3)
PW	59.0	0.9
CW	84.5	1.0
EVA	49.0	1.0
SA	75.0	0.9

The specific heat capacities of feedstocks were calculated from (4.1) using the DSC thermograms obtained with feedstocks, a standard material, and an empty pan.

$$Cp_{feedstock} = Cp_{standard} \cdot \frac{D_1 \cdot W_{standard}}{D_2 \cdot W_{feedstock}} \tag{4.1}$$

Where $Cp_{(feedstock)}$ is the specific heat capacity of the feedstock, $Cp_{(Standard)}$ is the specific heat capacity of the standard material (i.e., sapphire), D_1 is the heat flow difference (in $W \cdot g^{-1}$) between the DSC profiles obtained with the empty pan and feedstock, D_2 is the heat flow difference (in W·g -1) between the DSC profiles obtained with the empty pan and the standard material, Wfeedstock is the mass of feedstock, and Wstandard is the mass of the standard material (ASTM-E1269, 2018). The rheological behavior of the feedstocks was characterized using an Anton Paar MCR 302 rotational rheometer with a CC-17 concentric cylinder and a C-PTD 200 Peltier temperature-controlled measuring system. Molten feedstocks were poured into the cylinder, and then tested at shear deformation rates ranging from 0.5 to 3500 s^{-1} at three different temperatures (80, 90, and 100 °C). Each testing condition was repeated three times with different molten samples. The moldability of the feedstock was calculated using the moldability index model according to (4.2).

$$\alpha_{stv} = \frac{10^5}{\eta_0} \cdot \frac{|n-1|}{E/R} \tag{4.2}$$

Where αstv is the moldability index, η_0 is the viscosity at a reference shear rate representing the molding process (viscosity at 100 s^{-1} in this project), n is the flow behavior index, E is the activation energy for viscous flow, and R is the gas constant. This simple model was initially developed to compare the molding performance of plastic (Weir, 1963), and was recently introduced in HPIM and LPIM to assess the molding potential of feedstocks (Choi, Lyu, Lee, & Lee, 2014; Ghanbari, Alizadeh, Ghasemi, Rad, & Ghaffari, 2015; J Hidalgo, Jiménez-Morales, & Torralba, 2012).

The segregation potential of the feedstocks was characterized using a PerkinElmer Diamond TG/DTA thermogravimetric analyzer (TGA) according to the method developed in (Demers, Turenne, & Scalzo, 2015), and recently refined in (Demers, Fareh, Turenne, Demarquette, & Scalzo, 2018). Each feedstock was poured into cylindrical hot molds (Figure 4.2a), maintained at 90 °C for three different time periods (1, 10, and 60 minutes), and rapidly cooled to room temperature to form a cylindrical green part (Figure 4.2b). Cubic specimens of about 1 mm^3 were then extracted from three different positions of the molded part (i.e., from the top, the

middle, and the bottom of the molded part) according to the pattern presented in Figure 4.2c. The specimens were placed in standard platinum pans and then heated from 20 to 800 °C (heating rate of 20 °C·min^{-1}) under high purity nitrogen purge gas (flow rate of 60 ml·min-1). The solid loading over the molded part was calculated from the TGA profiles according to the weight fraction of the remaining powder after binder burn-out at these three different positions within the molded specimens according to (3.3).

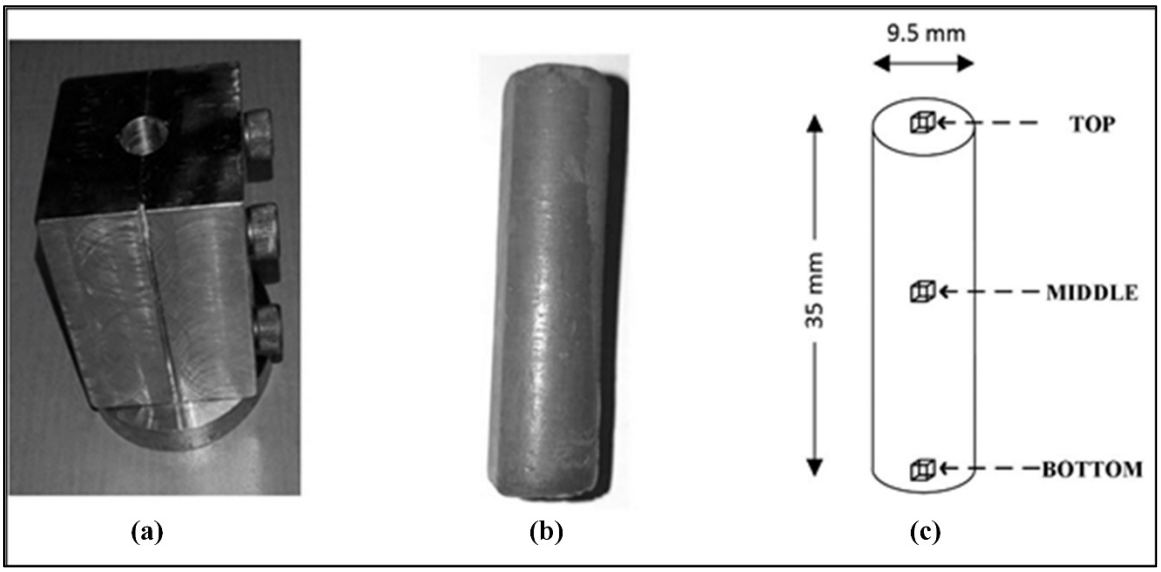

Figure 4.2 Specimen preparation for segregation tests: (a) mold for the cylindrical part, (b) typical cylindrical green part, and (c) position of the extracted specimens within the cylindrical green part for TGA tests

4.4 Results and discussion

4.4.1 Differential scanning calorimetry analyses

The differential scanning calorimetry profiles for different feedstocks are presented in Figure 4.3. Melting points of feedstocks were extracted from DSC thermograms, reported in Tableau 4.2, and finally used to set the minimum temperature for the rheological tests at 80 °C (i.e., slightly higher than the melting point) to guaranty the molten state of feedstocks. Comparison of melting points obtained with single-binder and multiple-constituents reported in Tableau

4.2 and Tableau 4.3 confirms that constituents have a certain degree of solubility together. Indeed, the mixture of carnauba wax with the other binder constituents produce a decrease of the melting point compared to the pure components (i.e., from 84.5 °C for carnauba wax vs 77.5 °C for feedstock).

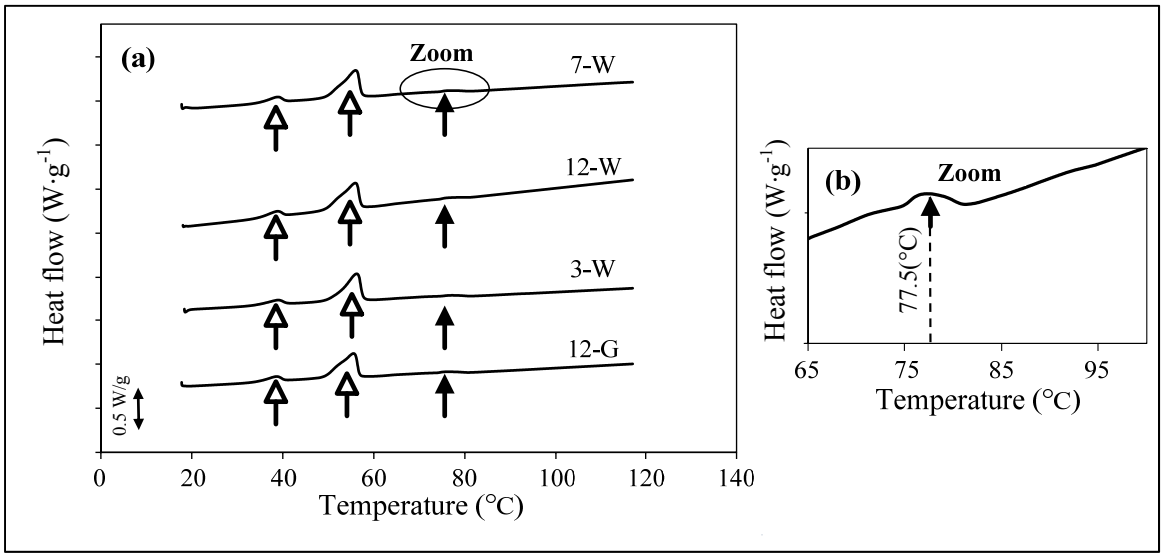

Figure 4.3 DSC results for (a) all feedstocks during heating, (b) zoom for identification of melting point

DSC thermograms were used to measure the values of the specific heat capacity (Cp), which are reported in Figure 4.4 for each feedstock. The values of the specific heat capacity of an injected feedstock present the quantity of heat added to or removed from the feedstock required to change the temperature during mold filling and solidification of the component. It is well accepted that the specific heat capacity can be estimated using a rule of mixture. This technique is widely used in composites to determine the Cp of a given composite material from the weight fraction and tabulated Cp of each constituent. Using this approach, the specific heat values are expected to be similar for all feedstocks used in this study since they were formulated using the same constituents (i.e., irrespective of the powder shape and size). However, for a given particle shape (e.g., water-atomized powder), the specific heat capacity of feedstock seems to increase with a decrease in particle size, with the feedstock 3-W generating a higher Cp value as compared to feedstock 12-W (Figure 4.4). In this respect, the 7-W mixture exhibits a specific

heat capacity value between those obtained with the feedstocks 3-W and 12-W. For the same particle size (i.e., d50 = 12 μm), the feedstock produced with the gas-atomized technique (feedstock 12-G) seems to demonstrate a higher specific heat capacity value than that produced with the water-atomized technique (feedstock 12-W), particularly in the liquid state (i.e., for the Cp values obtained at temperatures higher than 77.5 °C in Figure 4.4). The specific heat capacity measurement has received very little attention in the literature, and this impact of the particle size and the atomization technique must be confirmed in future works.

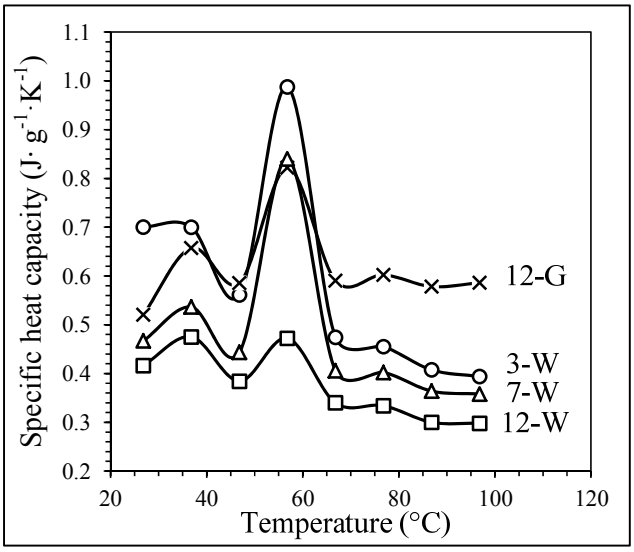

Figure 4.4 Specific heat capacity of feedstocks according to temperature

4.4.2 Rheological behavior of feedstocks

The rheological behavior obtained at three different temperatures is reported in Figure 4.5. All feedstocks are characterized by a near-Newtonian plateau observed at low shear rate (i.e., between 0.5 to 2 s^{-1}), followed by a clear and pronounced shear thinning behavior, where the viscosity decreases as the shear rate increases (i.e., between 2 and 3500 s^{-1}). At low shear rate, several feedstocks are characterized by a slight decrease in viscosity as the shear rate increases from 0. 5 to 0.9 s^{-1} , followed by a slight increase in viscosity as the shear rate increases from 0.9 to 2 s^{-1} (represented by a black arrow). Hausnerova et al. reported that this change from

pseudoplastic to dilatant behavior at low shear rate can be explained by the difficulty to form particle layers, which in turn results in particles sliding over each other and resulting in an increase in viscosity (Hausnerová et al., 2016; Hausnerová, Marcaníková, Filip, & Sáha, 2011). This "hook" phenomenon was observed for all temperatures used in this study. The second pseudoplastic behavior (i.e., the one observed from 2 to 3500 s^{-1} for all feedstocks) was explained by a restructuring of the mixture, with the alignment of polymer chains and particles as the shear rate increased. During the injection step of the LPIM process, this latter pseudoplastic behavior is generally suitable for promoting the mold filling. Figure 4.5 also indicates that the viscosity values of LPIM feedstocks depend on the temperature, powder size, and powder shape. The lowest viscosity value was obtained with feedstock 12-G, while the highest was achieved with feedstock 3-W. A high particle surface area measured with feedstock 3-W (reported in Table 1) is certainly linked to an amplification of the friction forces between the powder and binder leading to an increase in viscosity as compared to the other feedstocks. In the same vein, similar particle surface area values (varying between 0.08 and 0.10 $m^2 \cdot g^{-1}$) measured for the other three feedstocks are also in phase with the similar viscosity values obtained with these feedstocks. For the same powder size (i.e., 12-W vs. 12-G), the decrease in viscosity measured with feedstock 12- G may be attributable to a lower occurrence of irregularly shaped powder generally inherent to the gas atomization process.

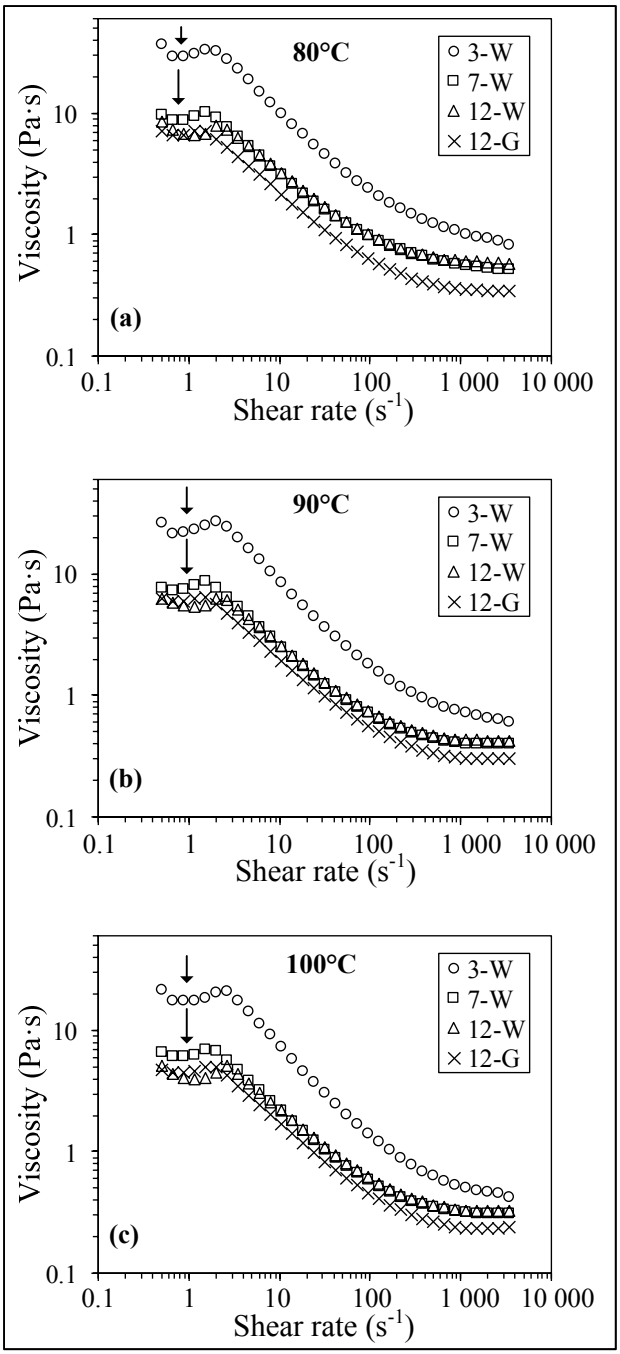

Figure 4.5 Viscosity profiles for 3-W, 7-W, 12-W, and 12-G feedstocks at 80, 90, and 100°C

Rheological parameters such as the reference viscosity (η_0), activation energy for flow (E), and shear sensitivity index (n) were extracted from Figure 4.5 using the same methodology detailed

in (V. Demers, 2017), and then plotted in Figure 4.6 In this context, the degree of temperature sensitivity to viscosity change was captured with the value of E, while the degree of shear rate sensitivity to viscosity change was quantified with the value of n. Although a viscosity change is expected with a change in temperature, a low value of E is suitable for minimizing sudden changes in feedstock viscosity between the hot and cold zones in the injection press or in the mold in order to minimize excessive residual stresses in green parts. For water-atomized feedstocks, the activation energy value decreases as the particle size increases. For the same powder size (i.e., 12-W vs. 12-G), the significant decrease in temperature sensitivity measured with feedstock 12-G may also be attributable to the lower interparticle contacts for particles exhibiting higher sphericity. As reported above, all feedstocks are characterized by a value of $n < 1$, indicating that the feedstock viscosity is strongly dependent on the shear rate. Generally, the value of this shear rate sensitivity index should be as small as possible to maximize the viscosity changes during and after the mold filling. The mixture, 3-W, has the smallest value of n, while the three other mixtures (7-W, 12-W, and 12-G) exhibit values of n ranging from 0.42 to 0.46, which can be considered similar as compared to the $n = 0.32$ obtained with feedstocks 3-W.

In this study, the capacity of the feedstock to be injected into the mold cavity was assessed through the calculation of the moldability index (α_{STV} presented in (3.2)), which was reported in Figure 4.6. This model combines the viscosity value with the shear rate and temperature sensitivity to predict the molding capability of feedstocks. From a molding perspective, the best feedstock candidate corresponds to the highest value of α_{STV} which is obtained for the lowest value of η_0, n, and E, concurrently. In this respect, feedstock 12-G demonstrates the best properties for the injection step of the LPIM process, while feedstock 3-W exhibits the least desirable moldability index value (Figure 4.6). The α_{STV} values obtained for feedstocks 7-W and 12-W are similar, indicating that a coarser powder (i.e., 12 vs. 7 μm) does not have a significant effect on the molding properties during injection. In the absence of an injection problem, the use of finer particles is generally suitable to minimize shrinkage during the sintering step of the process. The sinterability and moldability in this specific particle size distribution range will be studied in future works.

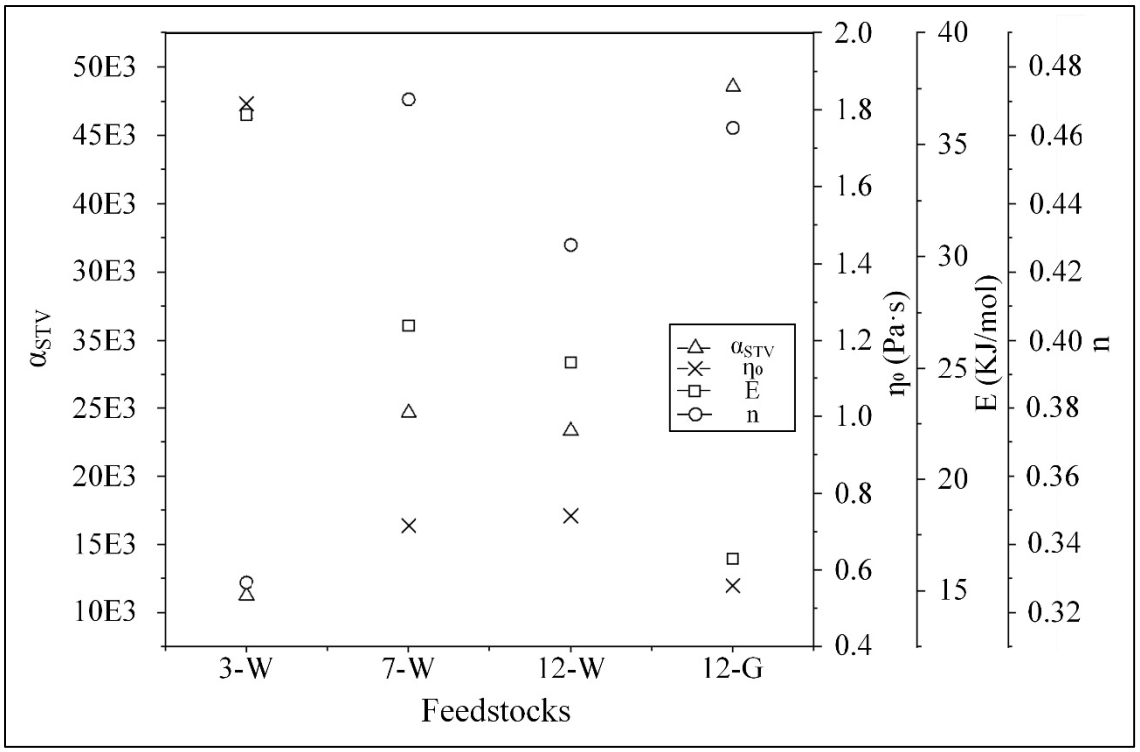

Figure 4.6 Moldability index (α_{STV}), reference viscosity at a reference shear rate of 100 s^{-1} (η_0), activation energy for flow (E), and shear sensitivity index (n) of feedstocks at 90 °C

4.4.3 Segregation analyses

Thermogravimetric analysis (TGA) was used to measure the weight fraction of the remaining powder after binder burn-out at three different positions within the molded specimens (i.e., top, middle, and bottom, according to the pattern presented in Figure 4.2c). Figure 4.7 presents a typical TGA profile obtained with feedstock 12-W, where the binder starts and ultimately burns around 175 °C and 400 °C, respectively. For convenience, the weight fraction of powder was converted in terms of volume fraction of powder using (3.3), and then compared to the nominal solid loading set at 60 vol. % in this study.

$$\text{vol.\%}_{\text{powder}} = \left[1 + \left(\frac{\rho_{\text{powder}}}{\rho_{\text{binder}}}\right) \cdot \left(\frac{1}{\text{wt.\%}_{\text{powder}}} - 1\right)\right]^{-1} \tag{4.3}$$

Where, vol. % powder is the volume fraction of powder, wt. %powder is the weight fraction of powder measured from the TGA profile, ρpowder is the density of the powder, and ρbinder is the density of the binder, with these latter values reported in Tableau 4.1 and Tableau 4.3.

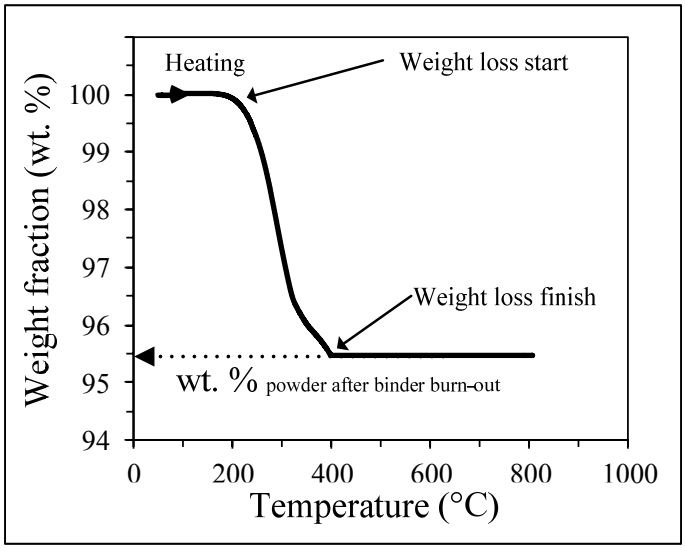

Figure 4.7 Typical TGA curve obtained with feedstock 12-W (bottom region of the molded specimen and maintained for 60 min in the molten state; c.f. Fig. 2c)

Segregation profiles representing the evolution of the volume fraction of powder according to the locations within the molded part are presented in Figure 4.8 according to the powder size, powder shape, and time spent in molten state. Our previous work showed that a measurement sensitivity of about +/- 0.25 vol. % can be considered for the detection of a real change in local solid loading using the TGA technique (V Demers et al., 2018). In other words, all feedstocks exhibiting solid loading values outside the 60.0 +/- 0.25 vol. % range can be considered as segregated mixtures. In this respect, all solid loading values above or below 60 vol. % represent a powder rich or a binder rich zone, respectively. The nominal solid loading is represented by a dashed line in Figure 4.8. For 1 min spent in molten state, no significant segregation was observed within the molded parts for all feedstocks (i.e., < 0.23 vol. % of powder). This result confirms that the binder formulation is well-adapted for standard injection conditions with all powders used in this study. For 10 min spent in molten state, the magnitude of segregation

remains insignificant for feedstock 3-W, while phase separation occurs at the top and bottom positions for the other three feedstocks. The intensity of segregation measured within feedstocks 7-W and 12-W is about 2-4 percentage points (lack/excess of powder), and this value increases up to 10 percentage points in excess of powder for feedstock 12-G (i.e., an important powder rich zone located at the bottom for feedstock 12-G as compared to feedstocks7-W and 12-W). Assuming that the driving force underlying this type of powder-binder segregation is gravity, the interparticle friction force is the mechanism opposing this segregation, which will thus be weakened as the powder sphericity increases from feedstocks 12-W to 12-G (i.e., similarly to the viscosity results presented above in Figure 4.5). The segregation during pouring is assumed negligible since the results obtained after 1 min in the liquid state did not exhibit segregation. For 60 min spent in molten state, the segregation measured within feedstock 3-W was below 1.4 percentage points (lack/excess of powder). This segregation magnitude is very low, considering that the three other feedstocks exhibit a significant difference in solid loading between the top, the middle, and the bottom regions.

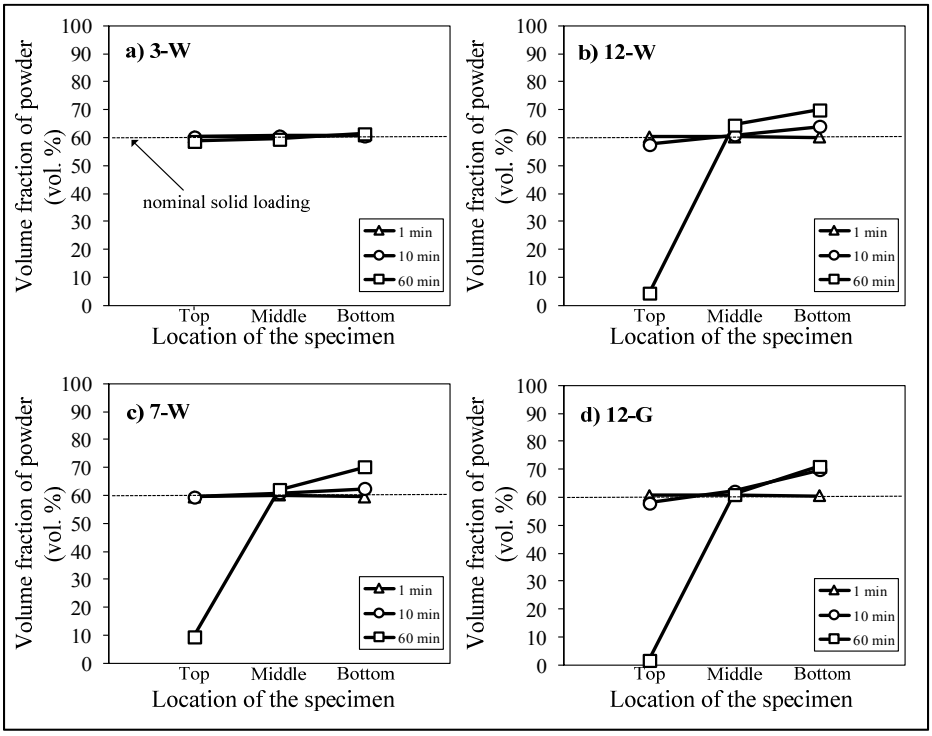

Figure 4.8 Volume fraction of powder according to the position, time left in the molten state, and feedstock

Representative SEM images (Figure 4.9) taken at different positions within the green part with feedstocks 3-W and 12-G were used to illustrate the powder/binder distribution at different locations. Figure 4.9a-c confirm that fine powder is well-distributed along the molded part. After a long time period in the molten state, the solid loading values (varying from 2 to 10 vol. % of powder) measured in the top region of feedstocks 7-W, 12-W, and 12-G confirm a binder-rich zone in which all powders move down over a distance of about 1.2 mm (visible in Figure 4.9d). Conversely, the highest solid loading values (converging to the same upper limit of about 70.2 to 71.3 vol. % of powder) were obtained with the three coarse powder feedstocks, 7-W, 12-W, and 12-G. In this respect, SEM images taken in the middle and the bottom regions of feedstock 12-G (Figure 4.9e, f) illustrate a slight increase in powder loading between these two positions within the molded part. Our previous work showed that this maximum value obtained at the bottom location corresponds to the critical solid loading, where all particles are in contact with each other, and the binder just fills the remaining interstices as illustrated in Figure 4.9f. From a practical perspective, an ideal feedstock should be easy to mold, generate no segregation after injection, and minimize shrinkage after sintering. On the one hand, feedstock 12-G can be considered the best candidate as it demonstrates the highest moldability properties, a low segregation potential if the mixture is injected within 1 min, and a typical powder size used in metal injection molding, i.e., where shrinkage could be managed in production (this latter point was not tested in this work). On the other hand, the very low segregation potential obtained with feedstock 3-W over any time period spent in molten state could pave the way for future developments of low viscosity feedstocks (e.g., < 0.1 Pa·s) using very low viscosity binder to increase moldability, and fine powders to increase sinterability.

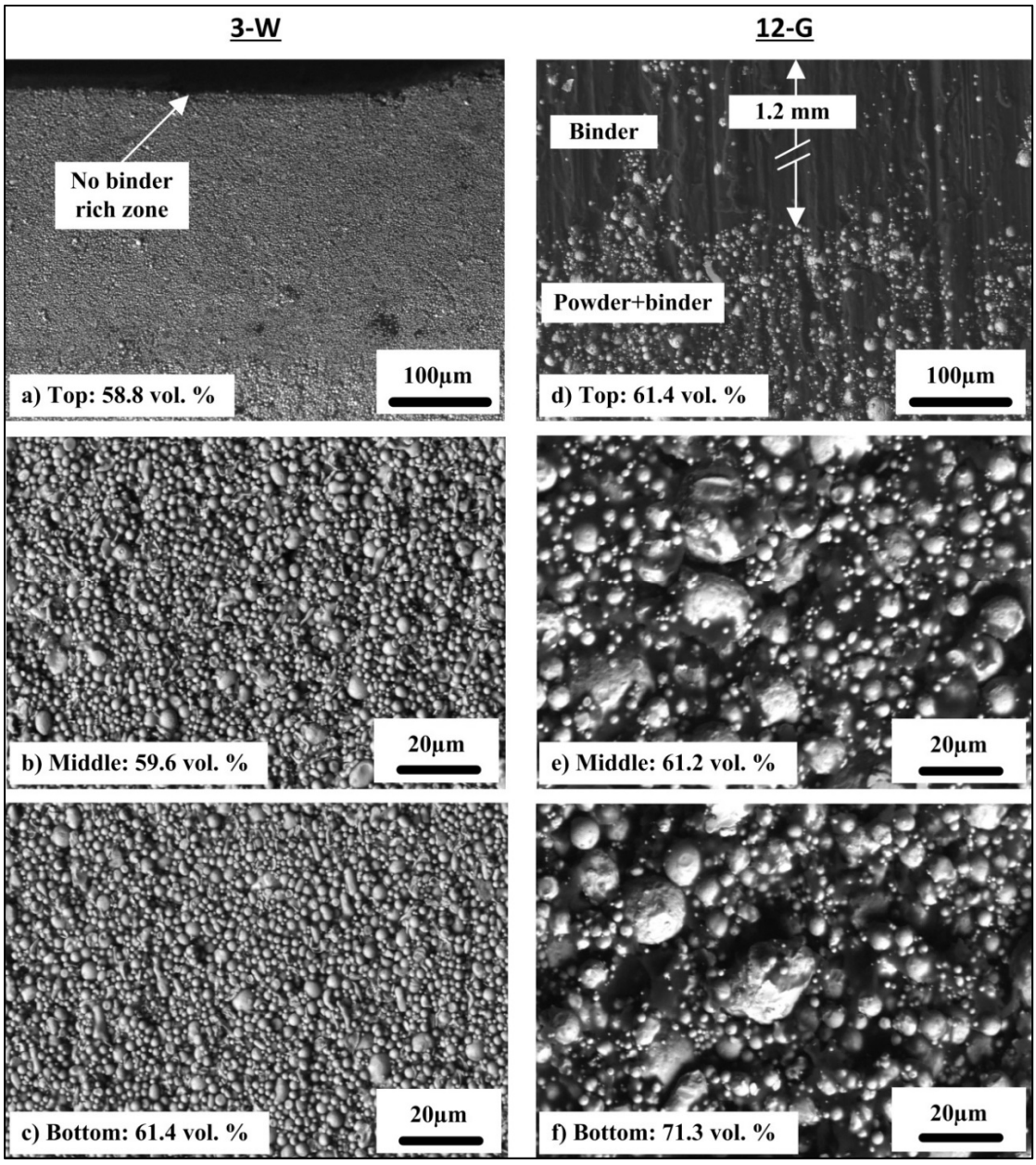

Figure 4.9 SEM images (BSE) representing the powder and binder distribution within feedstocks 3-W and 12-G at the top, middle, and bottom locations of the cylinder (60 min spent in molten state)

4.5 Conclusion

The influence of particle size and particle shape on rheological, thermal, and segregation properties was investigated for typical 17-4 PH feedstocks used in a low-pressure powder

injection molding process. The Weir's model was used to compare the feedstocks and to predict the impact of powder characteristics on the moldability capability of feedstocks. In contrast to the simple model using a rule of mixture, it was shown that the specific heat capacity is affected by the particle size as well as by the particle shape. As expected, the lowest and highest viscosity values were obtained with the largest and smallest powder size, respectively. The shear thinning behavior, generally suitable for the LPIM process, was observed over the main shear rate range for all feedstocks, irrespective of the powder size or powder shape because this phenomenon is manly driven by binder molecules' orientation and ordering with flow. It was also shown that the viscosity value is influenced by the sphericity of powder, with water-atomized powders producing more interparticular friction as compared with gas-atomized powders, which generate higher feedstock viscosity. Segregation results confirm that the binder formulation used in this study was well-adapted for standard injection conditions (i.e., using reduced time spent in molten state) with all powder lots. On the one hand, an increase in time spent in the molten state clearly has a detrimental effect on segregation, particularly for the feedstocks formulated with coarse powders (i.e., 7-W, 12-W, and 12-G). On the other hand, the very low segregation effects measured with feedstock 3-W during any time spent in the molten state pave the way for the future development of a new generation of LPIM feedstocks which are insensitive to segregation. From an injection perspective, it was shown that the feedstocks formulated with coarser and higher spherical particles (i.e., feedstock 12-G in this project) have a higher moldability potential. However, the similar moldability indexes obtained for feedstocks 7-W and 12-W indicate that a coarser powder (d50 = 12 vs. 7 μm) does not have a significant effect on the molding properties during injection. Since finer particles are generally suitable at the sintering stage of the process, this combined injection/sintering potential of such mixtures must be confirmed for irregular and spherical particles in future work.

4.6 Acknowledgements

This work was carried out with the financial support of the MITACS Globalink Graduate Fellowship and AeroCREATE Program in Competitive Manufacturing for the Aerospace Industry. The authors wish to thank Mr. O. Ghanmi for his collaboration in testing.

CHAPITRE 5

ARTICLE #2: NUMERICAL SIMULATION AND EXPERIMENTAL INVESTIGATION OF MOLD FILLING AND SEGREGATION IN LOW-PRESSURE POWDER INJECTION MOLDING OF METALLIC FEEDSTOCK

Mohamed Aziz Ben Trad [1], Vincent Demers[1*], Raphaël Côté[1], Mehran Sardarian[2], Louis Dufresne[1]

[1] École de technologie supérieure, 1100 Notre-Dame West, Montreal, QC, H3C 1K3, Canada
[2] Faculty of Materials and Metallurgical Engineering, Semnan University, 35131-19111, Semnan, Iran

Article soumis pour publication, octobre 2018

5.1 Abstract

Injection is one of the most important stages of the low-pressure powder injection molding process for which different types of defect may occur. The mold filling stage for low-pressure powder injection molding process and homogeneity of the injected part were simulated by finite element method and validated by an experimental approach. The numerical simulations were performed using Autodesk Moldflow Synergy 2019 package to investigate the injected length, the front velocity, the filling time, the shear rate, and to assess the magnitude of powder segregation after an injection. In this study, thermal and rheological characteristics of feedstock were experimentally measured to establish the constitutive equations required for the numerical model. Numerical simulation results were validated with real-scale injections (feedstock temperatures varying 80-100°C) using a laboratory injection press. Experimental characterization and injection campaign were conducted using a feedstock formulation based on 17-4 PH stainless steel powder (60 vol. % of powder) combined with a low-viscosity binder system. The injected length, the melt front velocity, the filling times, and the pressure predicted by the numerical model were in good agreement with the experimental observations with relative difference varying from 3.1 to 4.4%. Since the injections were performed and simulated at constant volumetric flow into a constant cross section mold cavity, the mold filling results confirm that the feedstock temperature has no influence on the injected lengths. The

segregation occurring during injection was also captured by this commercial software where experimental measurements of the local solid loading confirm the capability of the numerical model to predict successfully the homogeneous distribution of the powder (i.e., no segregation) within a simple shape mold cavity. Theses interesting simulation capacity in terms of injection behavior and segregation obtained for a simple shape green metallic components must be demonstrated for more complex shape part in future works. Although, the simulated injected lengths using different short shot conditions were in good agreement with the experimental observation (relative difference < 6%), the simulation results were not able to captured a slight increase in injected length obtained after real-scale injection for different feedstock temperatures. After an injection at low pressure, the powder-binder mixture was homogeneous since no segregation was predicted and measured through the injected green part. Short injection tests (3 s and 6 s) were achieved to mark the injected length in different temperatures. The velocity of the melt front and the injected length (e.g. 3 s and 6 s) increase marginally with the raise of the temperature from 80°C to 100°C. The analogy between simulation and real injection tests illustrated good similarity. The Moldflow synergy 2019 (Autodesk) solution was successfully validate with experimentation.

Keywords: Low-pressure powder injection molding, feedstock, simulation, viscosity, segregation, mold filling.

5.2 Introduction

Powder injection molding is a highly approved process for the mass-production of net-shape, precise, and complex shapes ceramic and metal parts. The PIM process involves four main stages including mixing powder with molten binder to obtain a feedstock, injection molding of the feedstock into a mold cavity, debinding to remove completely the binder (catalytic, solvent, or thermal debinding), and sintering under different atmospheres to obtain a final dense metallic or ceramic component (D. Heaney, 2012). Over the past 30 years, the conventional high viscosity feedstocks (e.g., 103 Pa·s, typically injected at pressure varying from 50 to 200 MPa) have been modified to develop low viscosity feedstocks suitable for the

low-pressure powder injection molding process (LPIM) injected at pressure generally lower than 1 MPa. The viscosity value of this new generation feedstocks is typically in the range of 1 to 20 Pa·s (Cetinel & Bauer, 2013), but generally lower than 10 Pa·s to accommodate the LPIM press using air pressure (J. Hidalgo, Abajo, Jimenez-Morales, & Torralba, 2013). The main advantages of the LPIM are associated to the low production cost combined with the flexibility to design very high complex shapes components (Medvedovski & Peltsman, 2013).

The injection is one of the most important stages of the process for shaping the part while avoiding defects such as sinks, voids, dead zones, warpage, cracks, and welding lines. The computer aided engineering has been successfully used to numerically simulate the injection molding stage of the conventional high-pressure powder injection molding (HPIM) for metal and ceramic. Initially developed for the production of ceramic components, the LPIM process has been adapted for the fabrication of metallic parts in the aerospace and medical industries (Ibrahim et al., 2012).Simulation of mold filling including filling time and filling pressure were realized with Moldflow Synergy for alumina-based feedstock (M. Sardarian, O. Mirzaee, & A. Habibolahzadeh, 2017b). This software package was also used to optimize the injection parameters for the fabrication of a complex shape zirconia ferrule (Zhang & Lin, 2007). Sardarian et al. have also shown the powerful capacity of computer aided engineering by simulating jetting phenomena and by predicting it relevance according to the injection temperature and pressure using Moldflow Synergy package (M. Sardarian, O. Mirzaee, & A. Habibolahzadeh, 2017a). Although some numerical simulation approaches were developed to predict the flow behavior of ceramic-based LPIM feedstocks, numerical models describing the injection stage using metallic-based LPIM feedstocks has received very little attention and was not demonstrated in literature. Simulation provides engineers a numerical feedback and guidelines to anticipate the flow behavior of the feedstock during the injection process in order to define the location of the injection gate, to select the appropriate materiel to set the process parameters leading in a minimization of the real-scale injections using the full empirical trial and error technique. The aim of this study is to simulate the mold filling behavior of metallic-based feedstock.

5.3 Experimental procedures

5.3.1 Feedstock preparation

A feedstock with 60 vol. % of metallic powder was prepared from stainless steel powder and wax-based binder. Gas-atomized 17-4PH stainless steel powder (Sandvik Osprey, United Kingdom) with a spherical shape and a nominal particle size of 12 µm was selected due to its extensive use in several sectors such as aerospace, medical, chemical, petrochemical, and food processing industries. A scanning electron microscope (Hitachi 3600, secondary electrons detector) was used to qualitatively evaluate the particle shape of each dry powder lot (Figure 5.1a). The particle size distribution and specific surface area were measured using an LS 13320 Beckman Coulter laser diffraction particle analyzer. The frequency curve and cumulative particle size distribution were plotted in Figure 5.1b and powder characteristics were reported in Tableau 5.1.

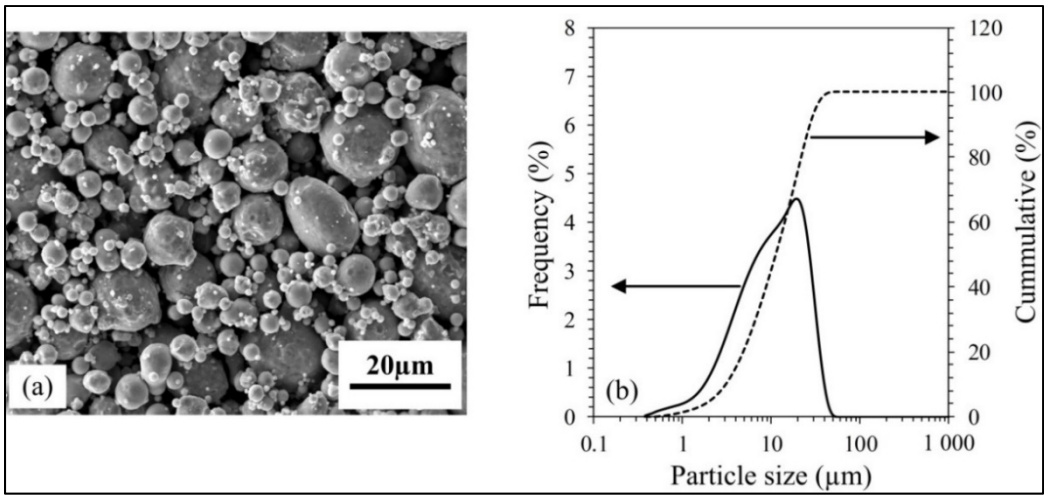

Figure 5.1 (a) SEM micrograph, and (b) particle size distribution (frequency and cumulative) of 17-4PH dry powder

The powder lot was combined with molten binder (80°C) in a laboratory planetary mixer for 45 minutes under vacuum to promote powder coverage, remove air bubbles, and produce homogeneous feedstock. In this study, the solid loading was set slightly lower than the critical

solid loading proposed by Hausnerova et al. for similar feedstock formulation in order to guarantee a proper fluidity of the powder-binder mixture during the injection stage (Hausnerova et al., 2017).

Tableau 5.1 Characteristics of 17-4PH powder

Density (g/cm^3)	**d_{10} (µm)**	**d_{50} (µm)**	**d_{90} (µm)**	**Specific surface area (m^2/g)**	**Supplier**
7.8	3.0	11.3	27.5	0.09	Osprey

The binder was formulated from four constituents in the proportion of 30 vol. % of paraffin wax, 7 vol. % of carnauba wax, 2 vol. % of stearic acid, and 1 vol. % of ethylene vinyl acetate. The melting points and density of each single binder constituent are given in Tableau 5.2. The paraffin wax was chosen due to the common use in the low-pressure injection molding process (Leverkoehne, Coronel-Hernandez, et al., 2001). The Carnauba wax was added into the binder for its lubricant and internal mold release properties (Majewska-Glabus, Zhuang, Vetter, & Duszczyk, 1995a). The stearic acid and ethylene vinyl acetate were selected as the surfactant and thickening agents, respectively (Li, Liu, Luo, & Yue, 2007).

Tableau 5.2 Melting points and density of the binder constituents

Binders	Melting point (°C)	Density (g/cm^3)
Paraffin wax)	59.0	0.9
Carnauba wax (CW)	84.5	1.0
Stearic acid (SA)	75.0	0.9
Ethylene vinyl acetate (EVA)	49.0	1.0

5.3.2 Measurement of the material properties

The rheological behavior of the molten feedstock was characterized using an Anton Paar MCR 302 rotational rheometer with a CC-17 concentric-cylinder and a C-PTD 200 Peltier temperature-controlled measuring system. Molten feedstock was poured into the cup of the rheometer and the mandrel was introduced into the molten mixture to apply shear deformation rates ranging from 0.5 to 3500 s^{-1} using different samples maintained at 80, 90, and 100 °C. Each condition was repeated three times at each temperature and the average value of the viscosity at each shear rate was used to plot the viscosity profiles of feedstock.

Melting points and specific heat capacity were obtained with a PerkinElmer Pyris 1 differential scanning calorimeter (DSC). Feedstock specimen and sapphire specimen were encapsulated in standard aluminum hermetic pans and tested over temperature ranging from 20 to 120 °C using a heating rate of 10 °C/min under dry nitrogen gas flow of 50 ml/min. The DSC thermograms were recorded from the second heating cycle to minimize the thermal history and to maximize thermal contact between the pan and specimen according to the standard test method (ASTM-D3418, 2015). The specific heat capacities of feedstock at different temperatures were calculated from the (5.1) using the three experimental DSC thermograms obtained with the feedstocks, a standard material (i.e., sapphire), and an empty pan according to the standard test method and reported in Figure 5.5 (ASTM-E1269, 2018).

$$Cp_{feedstock} = Cp_{standard} \cdot \frac{D_1 \cdot W_{standard}}{D_2 \cdot W_{feedstock}} \tag{5.1}$$

Where $Cp_{feedstock}$ is the specific heat capacity of the feedstock, Cpstandard is the specific heat capacity of the standard material, D1 is the heat flow difference between the DSC profiles obtained with the empty pan and feedstock, D2 is the heat flow difference between the DSC profiles obtained with the empty pan and the standard material, Wfeedstock is the mass of feedstock, and Wstandard is the mass of the standard material.

Density of the feedstock was measured by the Archimedes technique using a Sartorius YDK03 density kit according to the standard test method (ASTM-B311, 2017). The density of

feedstock at room temperature was calculated from the (5.2) using the mass of specimen taken in air and then in water.

$$\rho_{feedstock} = \frac{m_{air} \cdot \rho_{water}}{m_{air} - m_{water}} \tag{5.2}$$

Where $\rho_{feedstock}$ is the density of the feedstock, ρ_{water} is the density of water at given temperature, m_{air} is the mass of specimen in air (i.e., in dry condition), and m_{water} is the mass of specimen when immersed in water with the mass of specimen support tarred before the measurement.

The thermal diffusivities of feedstock at different temperatures were obtained by the laser flash method using a NETZSCH LFA 447 NanoFlash system according to the standard test method (ASTM-E1461, 2013). A thin circular specimen (Ø12.5 mm and 1.5 mm thick) was placed inside the apparatus to receive the energy of the pulse on the front face of the specimen and record the temperature on the rear face. The thermal diffusivity is established according to the time required to reach the front face temperature and the thickness of the specimen. In this study, the thermal diffusivity was measured only in solid state. The thermal conductivities were then calculated from the (5.3) and reported in Figure 5.6.

$$K_{feedstock} = \rho_{feedstock} \cdot Cp_{feedstock} \cdot \alpha \tag{5.3}$$

Where $K_{feedstock}$ is the thermal conductivity of feedstock, α is the thermal diffusivity of feedstock, and $Cp_{feedstock}$ and $\rho_{feedstock}$ were defined above (calculated from (5.1) & (5.2)). Maxwell model was used to validate the latter experimental thermal conductivity obtained in solid state as well as to predict the thermal conductivity in liquid state using the (5.4) and reported in Figure 5.6.

$$K_{feedstock} = K_m \left[\frac{K_f + 2K_m + 2v_f(K_f - K_m)}{K_f + 2K_m - v_f(K_f - K_m)} \right] \tag{5.4}$$

Where $K_{feedstock}$ is the thermal conductivity of the feedstock, K_m is the thermal conductivity of the binder, K_f is the thermal conductivity of the powder, and v_f is the volume fraction of powder fixed at 60 vol. % of powder in this study.

Solid loading within the injected part was characterized using a PerkinElmer Diamond TG/DTA thermogravimetric analyzer (TGA) according to the method recently developed and refined in previous study (V Demers et al., 2018). Cubic specimens of about 1 mm3 were extracted from the injected part according to the pattern presented in Figure 5.3b. The specimens were placed in standard platinum pans and then heated from 20 °C to 800 °C with a heating rate of 20°C/min under nitrogen purge gas with a flow rate of 60 ml/min. The weight fraction of the remaining powder after binder burn-out was determined from the TGA profiles as illustrated in Figure 5.2 which was converted in terms of volume fraction of powder according to (5.5).

$$vol.\,\%_{powder} = \left[1 + \left(\frac{\rho_{powder}}{\rho_{binder}}\right) \cdot \left(\frac{1}{wt.\,\%_{powder}} - 1\right)\right]^{-1} \tag{5.5}$$

Where, $vol.\ \%_{powder}$ is the volume fraction of powder, $wt.\ \%_{powder}$ is the weight fraction of powder measured from the TGA profiles, ρ_{powder} is the density of the powder (given in Tableau 5.1), and ρ_{binder} is the density of the binder (given in Tableau 5.2).

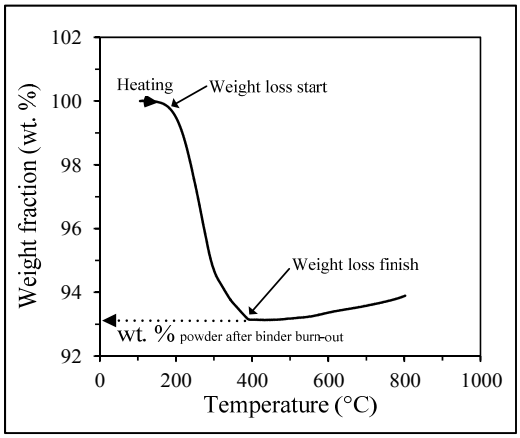

Figure 5.2 Typical TGA curve obtained from the position “A” c.f. Figure 5.3

5.3.3 Injection molding

Injections were performed using a laboratory injection press in which a new injection concept was developed to minimize segregation of low-viscosity feedstocks and to quantify the full moldability potential of the LPIM process (Lamarre, Demers, & Chatelain, 2017). Feedstock was heated up to 80, 90, or 100 °C, blended using a planetary mixer at 10 rpm for 15 minutes under vacuum, and then injected into a cylindrical mold cavity (Fig. 3a) with dimensions of Ø11.75 x 100 mm in length to produce green cylindrical parts (Figure 5.3b). A methodology for measuring in situ the filling pattern was adapted from the visualization method proposed by Pengcheng et al. by using a polycarbonate transparent plate used as one of the half of the mold to record the mold filling at different stages of the injection (Pengcheng, Fengxia, Zhiwei, Yumei, & Weimin, 2014). Virtual Dub was used to record the mold filling at 15 frames per second, while images data treatment was performed using Avimeca and Regressi as illustrated in Figure 5.3b. Between two injections, the feedstock remaining in the injection cylinder was returned into the container to be re-blended. The injection was performed using a controlled constant volumetric flow of 1.15 cm^3/s (value at the gate for a Ø15.9 mm) while the pressure value was recorded using a load cell located in the injection axe. The temperature of the molds was maintained at 35°C. Seven injections were run for each feedstock condition. Shear rate experienced by the feedstock during the mold filling was assessed using the analytical approach (5.6) often used in plastic injection molding (Rosato 3rd, 2000; Rosato, Rosato, & Rosato, 2000).

$$\dot{\gamma} = \frac{32Q}{\pi D^3} \tag{5.6}$$

Where $\dot{\gamma}$ is the shear rate, Q is the volumetric flow, and D is the diameter of the injected specimen.

5.3.4 Numerical simulation

Numerical simulations were performed using Moldflow Synergy 2019 (Autodesk Inc.). The cylindrical mold cavity was meshed using 3D tetrahedral-elements (as illustrated in Figure 5.3c and d, where the length of specimen was truncated for better clarity) containing 1,137,061 elements with an edge length of 0.6 mm proposing a good compromise between the accuracy of the results and an adequate time required for simulations. Feedstock properties listed in Tableau 5.3 were implemented in Moldflow. Since feedstock exhibit a shear thinning behavior, the matrix viscosity model was used to describe the evolution of viscosity according to the shear rate and temperature. The input parameters listed in Table 3 were arranged in terms of geometry, materiel properties, and operation parameters, while the output parameters were described as the injection length, the melt front velocity, filling time, shear rate and powder volume concentration according to our laboratory capability to experimentally validate each of these parameters.

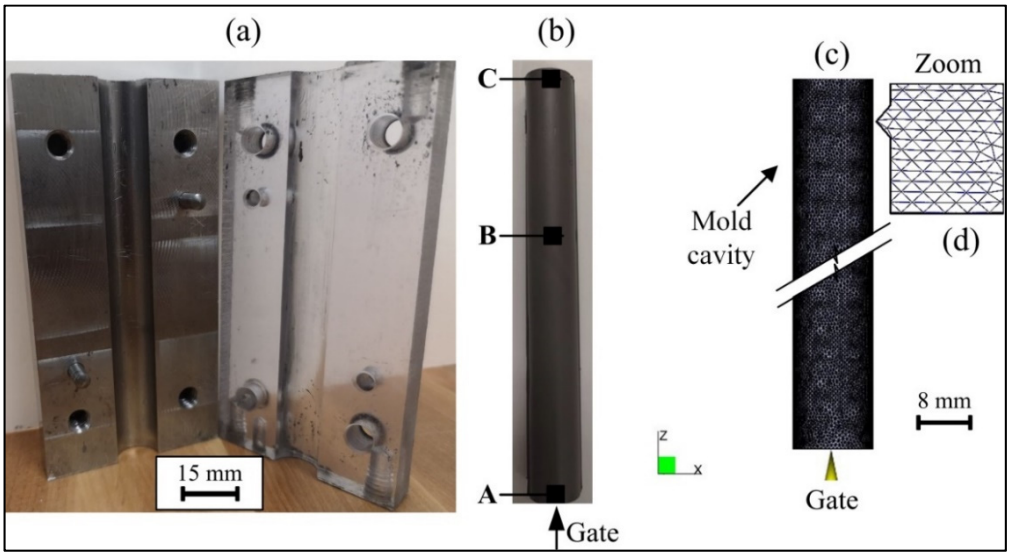

Figure 5.3 (a) mold for the cylindrical part, (b) typical cylindrical green part showing the positions of the extracted specimens for TGA tests, (c) representation of the cylindrical mold cavity with the superimposed tetrahedral finite elements mesh, and (d) zoom in the meshed specimen for visualization of the arrangement of tetrahedral-elements

5.4 Results and discussion

5.4.1 Feedstock properties

The differential scanning calorimetry thermogram for the feedstock is presented in Fig. 4a. The DSC curve exhibits three peaks corresponding to the fusion of different feedstock constituent's where the polymeric binder is completely melted at 77.5 °C (represented by a black arrow in Figure 5.5). The minimum temperature for the rheological tests was set at 80 °C (i.e., at slightly higher than the melting point) to guarantee the molten state of the feedstock. DSC thermograms were also used to measure the values of the specific heat capacity of feedstock as reported in Tableau 5.3. During the injection stage of the LPIM process, the values of the specific heat capacity present the quantity of heat added to or removed from the feedstock required to change the temperature during mold filling and solidification of the component. The open mark represents the calculated values of the specific heat based on the data available in the ASTM standard for the sapphire. The Cp values of feedstock slightly vary according to the temperature where values obtained before and after the fusion (i.e., Cp measured in solid and liquid states) are ranging from 0.52 to 0.58 J/g·K. From a comparison perspective, this value is in the same order of magnitude than that obtained for a high viscosity metallic-based feedstock (L. Kowalski, Duszczyk, & Katgerman, 1999) but about three times lower than that obtained for wax-based ceramic feedstock(M. Sardarian et al., 2017b). The specific heat capacity measurement of wax-based metallic feedstocks has received very little attention in the literature, and the impact of powder and binder characteristics on this thermal property should be investigated in future works.

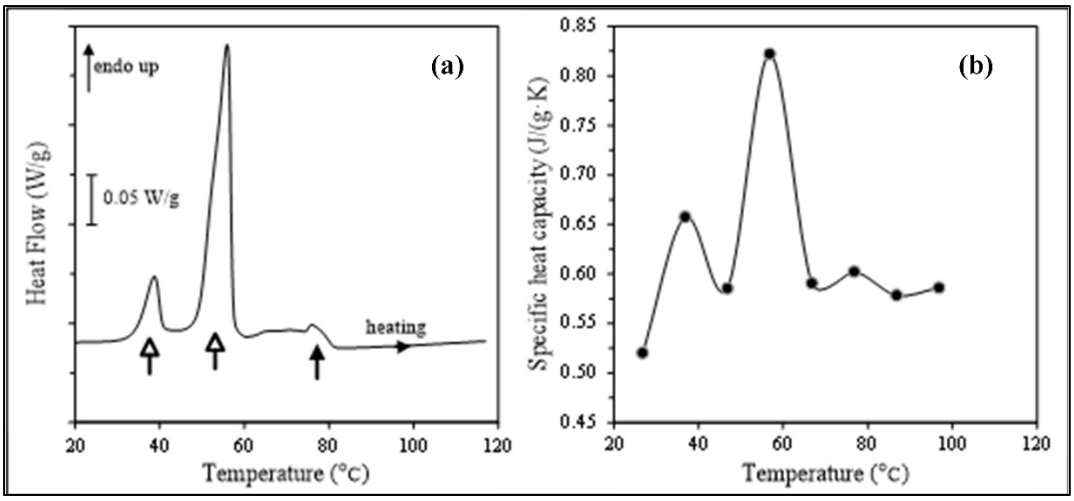

Figure 5.4 (a) DSC thermogram of feedstock obtained during the second heating cycle, and (b) specific heat capacity of feedstock measured at different temperatures

The viscosity profiles of the feedstock obtained at three different temperatures are reported in Figure 5.5. Each curve is constituted from 33 points of measurement but several marks were hidden for better clarity in Figure 5.5. The behavior of the powder-binder mixture is characterized by a first near-Newtonian plateau observed at low shear rate between 0.5 to 2 s^{-1}, followed by a clear shear thinning behavior between 2 to ~ 400 s^{-1} where the viscosity decreases as the shear rates increases, and a second near-Newtonian plateau observed at high shear rate for values > 400 s^{-1} where the viscosity varies sparsely for any further increase in shear rate. As expected, the viscosity values of this metallic-based feedstock depend also on the temperature where the lowest viscosity value was obtained at 100 °C. The influence of shear rate and temperature on viscosity was captured with a simple matrix model.

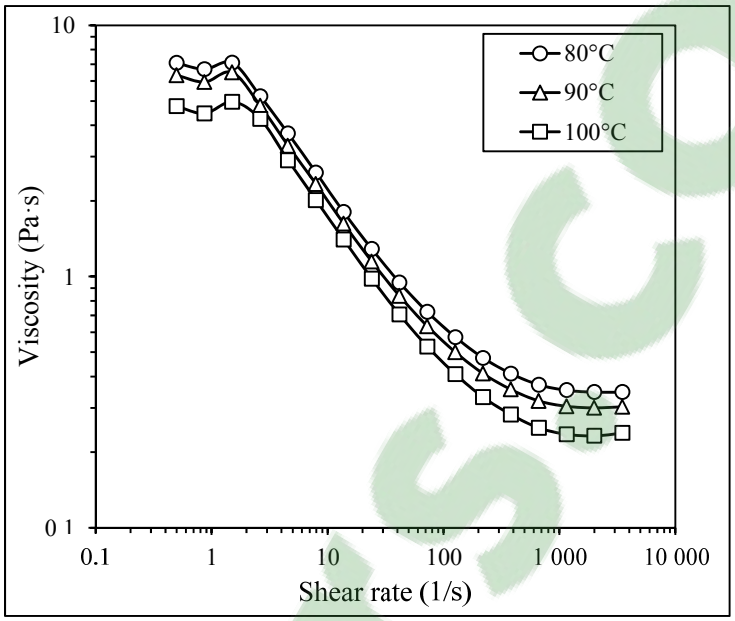

Figure 5.5 Viscosity profiles of the feedstock measured at 80, 90, and 100°C

The thermal conductivity of the feedstock measured at different temperatures is reported in Figure 5.6. The k value of feedstock seems to slightly decrease as the temperature increases. It can be realized that the experimental results converge to the value calculated with the Maxwell model (Figure 5.6). The thermal conductivities measured in the framework of this project are situated between the values calculated by Kowalski et al. (i.e., $k \approx 1.3$ W/m·K for the Maxwell model and $k \approx 4$ W/m·K for the Lewis & Nielson model) for a high viscosity metallic-based feedstock (L. Kowalski et al., 1999) and slightly higher than that calculated using the Maxell model with the estimated values of each single constituent (see (5.4)) as well as the thermal conductivity proposed by Sardarian et al. ($k \approx 1.5$ W/m·K) for wax-based ceramic feedstock (Sardarian et al., 2017). In general, the specific heat capacity as well as thermal conductivity measurements of wax-based metallic feedstocks have received very little attention in the literature, and the impact of powder and binder characteristics on this thermal properties should be investigated in future works.

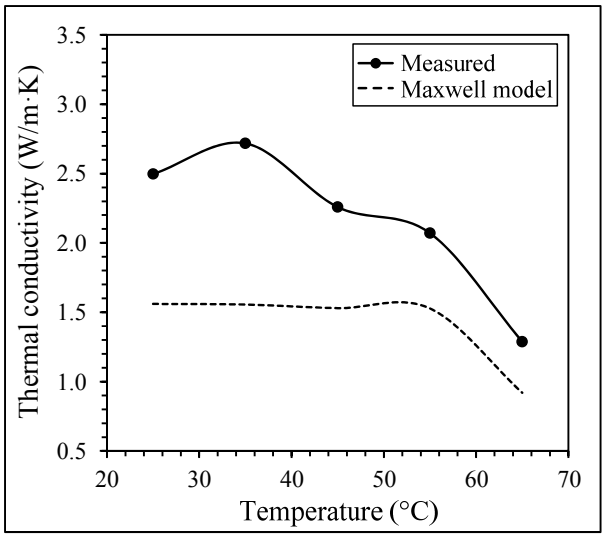

Figure 5.6 Measured and calculated thermal conductivity for feedstock

Tableau 5.3 summarized the material properties obtained experimentally in the framework of this study and data-fitted coefficients that were implemented in Moldflow for numerical simulations.

Tableau 5.3 Input data of feedstock obtained experimentally for the numerical simulation

Cp	at 27°C	0.5203 J/g·K	*k*	at 35°C	2.72 W/m·K
	37°C	0.6574 J/g·K		45°C	2.26 W/m·K
	47°C	0.5855 J/g·K		65°C	1.29 W/m·K
	57°C	0.8220 J/g·K		80°C	1.14 W/m·K
	67°C	0.5906 J/g·K		100°C	1.14 W/m·K
	77°C	0.6022 J/g·K	ρ		5.03 g/cm^3
	87°C	0.5783 J/g·K	T_m		77.5 °C
	97°C	0.5861 J/g·K			

5.4.2 Injected length, melt front velocity, and filling time

During the filling stage, the injected length increases at constant melt front velocity since the injection is performed at constant volumetric flow into a constant cross section mold cavity. Figure 5.7 presents the typical experimental and simulated injection results obtained with feedstock at 80°C after short shot injection tests (i.e., the process was stopped after 3 and 6 s) for calculation of the injected length. As seen in Figure 5.7a, no visual defect was detected at the surface of the molded parts after injections for all processing conditions, while the simulated injected lengths matched the experiment well. A look at the real-scale injections results revealed no significant change in injected length according to the feedstock temperature (Figure 5.7b). The standard deviation varying from 0.4 to 2 mm (reported in Figure 5.7b if visible compared to the size of the marks) shows the intrinsic variation of the process for average injected lengths obtained from seven injections and confirms that injected volumes after 3 and 6 s were constant irrespectively to the feedstock temperature. This constant injected length over the feedstock temperature was also predicted by the numerical model with a relative difference less than 3.1% between simulations and experiments results for all short shot tests and feedstock temperature.

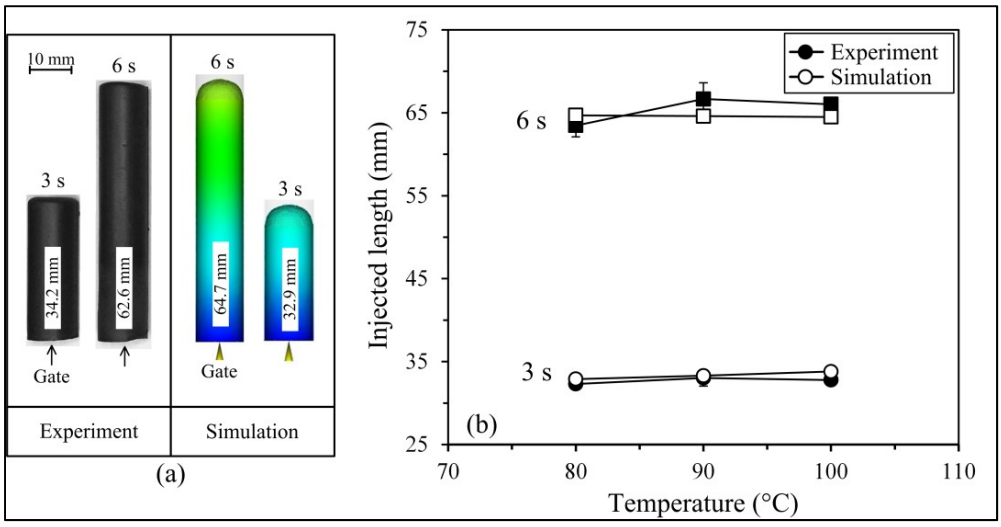

Figure 5.7 Experimental and simulated injected length (a) typical results after short shots of 3 and 6 s with feedstock at 80°C, and (b) injected length for different processing conditions

The setup used to record the evolution of the injected length using a transparent mold is shown in Figure 5.8a where the melt front velocity was captured using a superimpimposed scale in Avimeca and treated using the Regressi software. A velocity distribution ranging from 0.750 to 1.125 cm/s was simulated through the injected part as illustrated in Figure 5.8a. The average melt front velocity obtained experimentally and numerically for different feedstock temperatures was reported in Figure 5.8b. As expected for both experimental and simulation results, the melt front velocity is almost constant according to the temperature since all injections were performed at constant volumetric flow which is controlled by the injection press and not the feedstock properties. In this respect, a standard deviation of the experimental melt front velocity as low as 0.02-0.04 cm/s was calculated from the real-scale injections (not reported in Figure 5.8b because the error bars are lower than the size of the marks). The simulated melt front velocity at a given injection time was calculated from the average values along diameter and reported in Figure 5.8b to confirm that the model was closed to the experiment with a maximum relative difference of 4.4% between simulations and experiments results.

The filling time of the mold cavity is a parameter generally used for the optimization of the injection process in terms of productivity. For a constant volumetric flow injection, this parameter is directly derived from the melt front velocity and is also constant according to the feedstock temperature (Figure 5.8b). The filling times predicted by the numerical model were in good agreement with the experimental observations with a maximum relative difference of 3.8%. It is interesting to note that the filling times obtained in this study were significantly higher than those obtained with conventional LPIM press using air pressure to fill the mold cavity in few tenths of a second. A lower melt front velocity (i.e., a higher filling time) favors a laminar and calm mold filling resulting in the fabrication of defect-free parts (cavities, weld line, internal stresses, etc.). However, this injection approach may be too slow to fill properly thin sections or other complex shape features of the mold cavity since solidification rate could be faster than the melt front velocity that may turn in filling defects. This issue must be studied in future work to confirm this antagonistic effect between the filling time and molding defects, and establish the optimal filling time for complex shape parts.

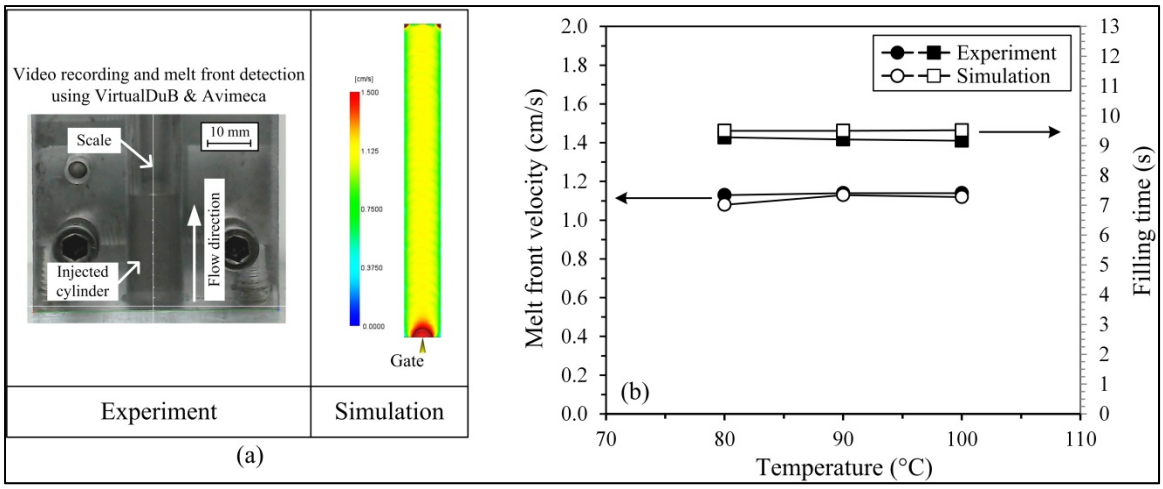

Figure 5.8 Experimental and simulated melt front velocity and filling time (a) typical results showing the melt front shape and methodology used to capture the melt front velocity, and (b) melt front velocity and filling time for different processing conditions

5.4.3 Shear rate

The simulated shear rate experienced by the feedstock during the injection is illustrated in Figure 5.9. For this cylindrical part, the model predicts a shear rate varying from 0 to 20 s^{-1} that may correspond to a change in viscosity ranging from 1 to 7 Pa·s for a non-Newtonian fluid such as wax-based feedstock illustrated in Figure 5.5. This decrease in viscosity could be amplified for a complex shape mold cavity where gradient in injection speed could be more pronounced than the one observed in the framework of this study with a simple shape component. Since distribution of shear rate cannot be measured experimentally in the mold, the analytical model described in (5.6) was used to calculate a shear rate ranging from 3 to 7 s^{-1} in the gate and in the mold, corresponding to similar values than those obtained with the numerical model. For a given mold cavity, an increase in injection speed (i.e., increase of Q in (5.6)) can be seen as an opportunity to increase the shear rate leading in a decrease in viscosity leading in an increase in moldability potential.

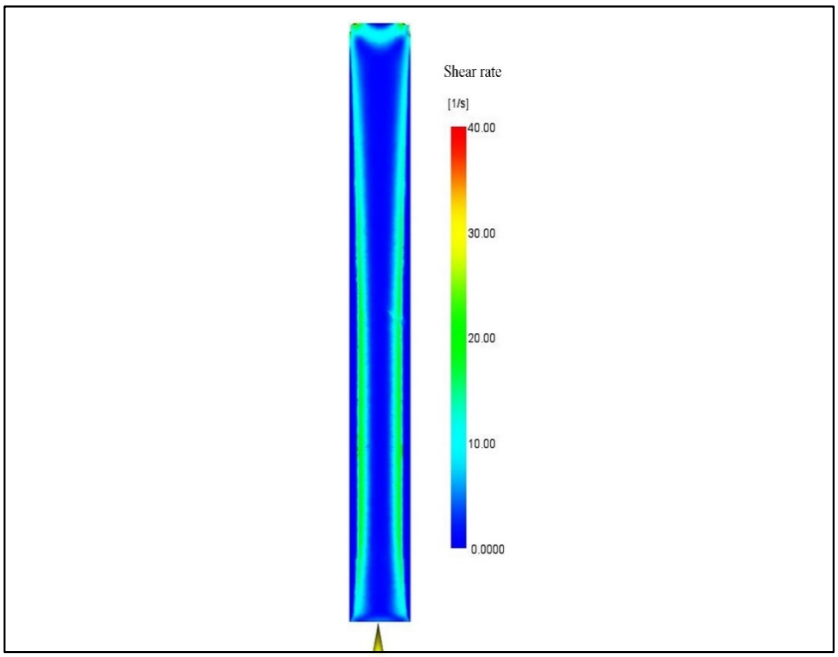

Figure 5.9 Simulation of shear rate at the end of the injection

5.4.4 Powder segregation analyses

Segregation of feedstock is an inhomogeneous distribution of powder particles by size, shape, density, or quantity. This undesirable effect in the powder-binder mixture is generated by an improper mixing method during feedstock preparation, high shear deformation rate gradients during the molding process, or by the gravity of feedstock that remains idle during the process dead times. This fluctuation of the particle distribution in feedstock may lead to distortions, cracks, voids, warping and heterogeneous shrinkage of the sintered parts.

The segregation occurring during injection was captured by Moldflow Synergy 2019 package and experimentally validated using thermogravimetric analysis. Simulation results presented in Figure 5.10a clearly predict that the injection process in this simple shape cavity produced no significant segregation through the green part. Indeed, the simulated distribution of powder through the injected part was mainly at the nominal solid loading of 60.0 vol. % except within thin zones characterized by a volume fraction of powder varying from 59.75 to 60.25 vol. % (represented by the colors yellow and cyan in Figure 5.10a). The thermogravimetric analyses (TGA) presented in Figure 5.10b confirm this numerical prediction where all measured solid

loading are within or just slightly out of the sensitivity limit of this experimental technique (the nominal solid loading is represented by a continuous line in Figure 5.10b). Indeed, our previous work showed that a measurement sensitivity of about +/- 0.25 vol. % (marked with dashed lines in Figure 5.10b) can be considered for the detection of a real change in local solid loading using the TGA technique (Demers et al., 2018). Therefore, all feedstocks exhibiting solid loading values inside the 60.0 +/- 0.25 vol. % range can be considered as non-segregated mixtures or simply below the detection limit of the method. This result confirms that the binder system formulation is well adapted for the low-pressure powder injection molding process. For this kind of simple shape cavity, no real segregation was expected as predicted by the numerical model with a relative difference below 1% compared to the experiments. It is thus proposed to test the potential of the segregation simulation package in future works to capture the impact of high shear deformation rate gradients during the molding process for more complex shape which are generally more sensitive to segregation.

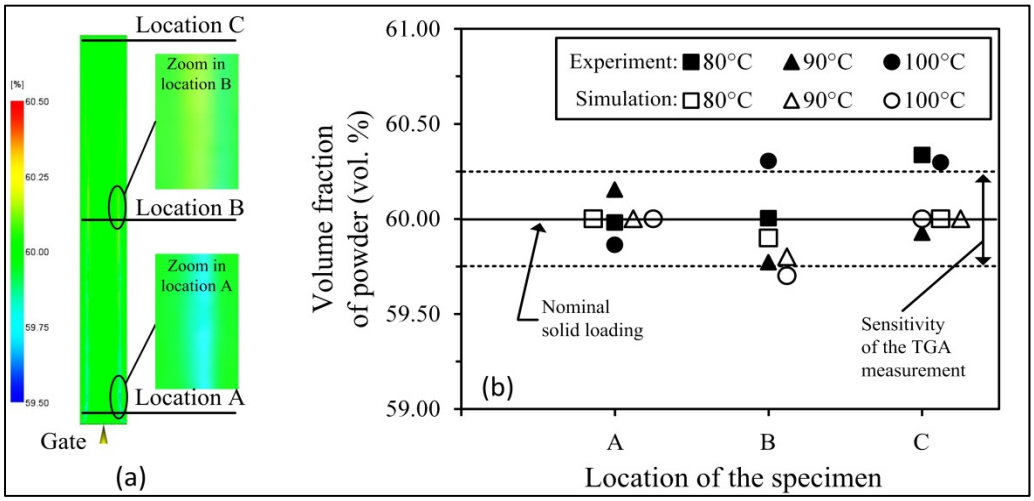

Figure 5.10 Volume fraction of powder through the green part (a) typical results from simulation, and (b) comparison of the simulation and experiment according to the position and feedstock temperature

5.5 Conclusions

The commercial package Autodesk Moldflow synergy 2019 was used to simulate the mold filling behavior of metallic-based feedstock with the low-pressure powder injection molding

process (LPIM). Experimental characterization and injection campaigns were conducted with feedstock formulated from 17-4 PH stainless steel powder and waxes-based binder system at a solid loading of 60 vol. % of powder. The feedstocks properties such as viscosity, melting point, thermal conductivity, density, and specific heat capacity were experimentally characterized to establish the constitutive equations required for the numerical model. Numerical mold filling simulation results were validated with real-scale injections using different feedstock temperatures while simulation of segregation after injection was validated using thermogravimetric analysis.

The injected length, the melt front velocity and the filling times predicted by the numerical model were in good agreement with the experimental observations with relative difference varying from 3.1 to 4.4 %. Since the injections were performed and simulated at constant volumetric flow into a constant cross section mold cavity, the mold filling results confirm that the feedstock temperature has no influence on the injected lengths. The segregation occurring during injection was also captured by this commercial software where experimental measurements of the local solid loading confirm the capability of the numerical model to predict successfully the homogeneous distribution of the powder (i.e., no segregation) within a simple shape mold cavity. Theses interesting simulation capacity in terms of injection behavior and segregation obtained for a simple shape green metallic components must be demonstrated for more complex shape part in future works.

5.6 Acknowledgements

This work was carried out with the financial support of the MITACS Globalink Graduate Fellowship and AeroCREATE Program in Competitive Manufacturing for the Aerospace Industry. The authors wish to thank Mr. V. Lechner and A. Durand for their collaboration in experimental injection tests.

CONCLUSION

L'objectif de ce projet de maitrise était d'étudier la phase d'injection par la mise en œuvre de simulations numériques et de validations expérimentales. Les conclusions détaillées spécifiques à chaque article scientifique se trouvent aux sections 4.5 et 5.6 présentées plus haut dans ce document. L'effet de la taille des particules et de la morphologie des poudres (atomisées à gaz vs atomisées à l'eau) sur les propriétés des mélanges pour l'injection des poudres métallique à basse pression a été étudié. Quatre différents mélanges ont été préparés pour mesurer leurs viscosités, leurs capacités thermiques, leurs moulabilités et l'effet de la ségrégation en fonction des caractéristiques des particules (i.e., taille et forme). Le but de cette première étude est de déterminer le meilleur mélange en termes de moulabilité pour l'étape d'injection. Le mélange 12-G (préparé avec la poudre atomisée au gaz ayant une taille moyenne de 12 μm) se distingue avec sa moulabilité élevée et son potentiel de ségrégation faible. Pour cette raison, ce mélange a été choisi pour réaliser l'étude de la simulation numérique avec Autodesk Moldflow Synergy 2019 de la phase d'injection et la validation expérimentale.

Les résultats obtenus dans le cadre de l'article 1 ont confirmé que la capacité thermique spécifique est affectée par la taille des particules ainsi que par la forme des particules. Comme prévu, les valeurs de viscosité les plus faibles ont été obtenues par les poudres avec un diamètre moyen d_{50} le plus grand. Du point de vue de l'injection, il a été montré que les matières premières formulées avec des particules sphériques et plus grossières (c'est-à-dire la 12-G dans ce projet) avaient un potentiel de moulabilité plus élevé. Cependant, les indices de moulabilité similaires obtenus pour les mélanges 7-W et 12-W indiquent qu'une poudre plus grossière n'a pas d'effet significatif sur les propriétés de moulage pendant l'injection

Les résultats expérimentaux obtenus dans le cadre de l'article 2 ont permis de valider les résultats de simulation numérique de l'injection des poudres métallique à basse pression avec des injections à l'échelle réelle. Le remplissage du moule lors de l'injection confirme que la température du mélange n'a pas d'influence sur les longueurs injectées. La ségrégation survenant au cours de l'injection a également été capturée par Moldflow Synergy 2019 dans

lequel des mesures expérimentales du chargement solide confirment la capacité du modèle numérique à prédire avec succès la distribution homogène de la poudre.

RECOMMANDATIONS

C’est très important de pousser la recherche plus loin dans ce domaine pour répondre à plusieurs autres questions. Par exemple, les mélanges 7-W et 12-W ne présentent pas de différence de point de vue injéctabilité. Ceci est un paramètre intéressant à étudier dans une étude future où la moulabilité et la frittabilité pourraient être comparées afin de bénéficier de l’effet d’une taille de particule plus fine (i.e., définir si la diminution de taille à 7 μm produit un impact significatif sur la frittabilité sans réelle diminution de la moulabilité avec cette poudre). Encore, la chaleur spécifique massique présente un défi important. La composition du mélange poudre-liant ne permet pas de prédire la valeur de Cp en fonction de la loi des mélanges comme les particules ne sont pas identiques (formes et tailles). Dans la littérature, il y a aussi un manque d’information. On trouve des valeurs de chaleur spécifique massique, mais on ne trouve pas des explications pour les mélanges utilisés en MIM. Encore, Une étude pour che4rcher la relation entre la conductivité thermique et la chaleur spécifique massique est très bénéfique pour prédire la diffusivité thermique qui nous permette de simuler la phase de refroidissement lors de l’injection.

Pour la partie de la simulation numérique, la capacité du logiciel en termes de comportement d'injection et de ségrégation obtenue pour une forme de piéce simple doit être démontrée pour des pièces de formes plus complexes dans les travaux futurs. Une pièce de forme géométrique complexe peut provoquer plus de défauts lors de l’injection. Comme les taux de cisaillements et les vitesses des fronts de matière dans les différentes directions sont variables en fonction de la géométrie, la concentration de la poudre, le temps d’injection et la forme de la pièce à un instant bien précis peuvent être investiguées afin de valider la performance de Autodesk Moldflow Synergy 2019.

LISTE DES RÉFÉRENCES BIBLIOGRAPHIQUES

Aslam, M., Ahmad, F., Yusoff, P. S. M. B. M., Altaf, K., Omar, M. A., Abdul Khalil, H., & Raza, M. R. (2016). Investigation of rheological behavior of low pressure injection molded stainless steel feedstocks. *Advances in Materials Science and Engineering, 2016*.

ASTM-B311. (2017). Standard Test Method for Density of Powder Metallurgy (PM) Materials Containing Less Than Two Percent Porosity, ASTM International, West Conshohocken, PA.

ASTM-D3418. (2015). *Standard Test Method for Transition Temperatures and Enthalpies of Fusion and Crystallization of Polymers by Differential Scanning Calorimetry, ASTM International, West Conshohocken, PA*.

ASTM-E1269. (2018). Standard Test Method for Determining Specific Heat Capacity by Differential Scanning Calorimetry, ASTM International, West Conshohocken, PA.

ASTM-E1461. (2013). Standard Test Method for Thermal Diffusivity by the Flash Method, ASTM International, West Conshohocken, PA.

Binet, C., Heaney, D. F., Spina, R., & Tricarico, L. (2005). Experimental and numerical analysis of metal injection molded products. *Journal of Materials Processing Technology, 164-165*, 1160-1166.

Cetinel, F. A., & Bauer, W. (2013). Ceramic micro parts. Part 1: How thermal debinding can be utilized to enhance surface finish and mechanical properties. *Journal of the European Ceramic Society, 33*(15-16), 3123-3134.

Choi, J.-P., Lyu, H.-G., Lee, W.-S., & Lee, J.-S. (2014). Investigation of the rheological behavior of 316L stainless steel micro-nano powder feedstock for micro powder injection molding. *Powder technology, 261*, 201-209.

Chung, C., Carpenter, B., Cao, M., Liu, C., & Rhee, B. (1990). Property Characterization of Feedstock for Powder Injection Molding. *Advances in Powder Metallurgy 1990., 3*, 247-282.

Contreras, J., Jimenez-Morales, A., & Torralba, J. (2010). Experimental and theoretical methods for optimal solids loading calculation in MIM feedstocks fabricated from powders with different particle characteristics. *Powder metallurgy, 53*(1), 34-40.

Costa, C., Michels, A., & Kipper, M. (2018). Welding lines formation in holes obtained by low pressure injection molding of ceramic parts. *Cerâmica, 64*(369), 97-103.

Demers, V., Fareh, F., Turenne, S., Demarquette, N., & Scalzo, O. (2018). Experimental study on moldability and segregation of Inconel 718 feedstocks used in low-pressure powder injection molding. *Advanced Powder Technology, 29*(1), 180-190.

Demers, V., Turenne, S., & Scalzo, O. (2015). Impact of binders on viscosity of low-pressure powder injection molded Inconel 718 superalloy. *Journal of materials science, 50*(7), 2893-2902.

Demers, V., Turenne, S., & Scalzo, O. (2015). Segregation measurement of powder injection molding feedstock using thermogravimetric analysis, pycnometer density and differential scanning calorimetry techniques. *Advanced Powder Technology, 26*(3), 997-1004.

Enneti, R. K. (2005). Thermal analysis and evolution of shape loss phenomena during polymer burnout in powder metal processing.

Fang, W., He, X., Zhang, R., Yang, S., & Qu, X. (2014). The effects of filling patterns on the powder–binder separation in powder injection molding. *Powder technology, 256*, 367-376.

Fareh, F., Demers, V., Demarquette, N. R., Turenne, S., & Scalzo, O. (2016). Molding properties of inconel 718 feedstocks used in low-pressure powder injection molding. *Advances in Materials Science and Engineering, 2016*.

Fareh, F., Demers, V., Turenne, S., & Scalzo, O. (2016). Segregation measurement of inconel 718 feedstocks used in low-pressure metal injection molding. Dans *Materials Science Forum* (Vol. 857, pp. 286-290). Trans Tech Publ.

Gelin, J.-C., Barriere, T., & Song, J. (2010). Processing defects and resulting mechanical properties after metal injection molding. *Journal of Engineering Materials and Technology, 132*(1), 011017.

German, R. (2012). Metal powder injection molding (MIM): key trends and markets. Dans *Handbook of metal injection molding* (pp. 1-25). Elsevier.

German, R. M., & Bose, A. (1997). *Injection Molding of Metals and Ceramics*. Metal Powder Industries Federation. Repéré à https://books.google.ca/books?id=jXINAAAACAAJ

Ghanbari, A., Alizadeh, M., Ghasemi, E., Rad, R. Y., & Ghaffari, S. (2015). Preparation of optimal feedstock for low-pressure injection molding of Al/SiC nanocomposite. *Science and Engineering of Composite Materials, 22*(5), 549-554.

Gholami, E., & Demers, V. Molding Properties of Cobalt-Chrome-Based Feedstocks Used in Low-Pressure Powder Injection Molding.

Hausnerova, B. (2011). *Powder injection moulding-An alternative processing method for automotive items*. InTech.

Hausnerová, B., Kasparkova, V., & Hnátková, E. (2016). Rheological and thermal performance of newly developed binder systems for ceramic injection molding. Dans *AIP Conference Proceedings* (Vol. 1736, pp. 020120). AIP Publishing.

Hausnerová, B., Kitano, T., & Sáha, P. (2010). Effect of particle size distribution on the flow behaviour of powder injection moulding materials. *Latest Trends on Engineering Mechanics, Structures, Engineering Geology*.

Hausnerová, B., Marcaníková, L., Filip, P., & Sáha, P. (2011). Optimization of powder injection molding of feedstock based on aluminum oxide and multicomponent water-soluble polymer binder. *Polymer Engineering & Science, 51*(7), 1376-1382.

Hausnerova, B., Mukund, B. N., & Sanetrnik, D. (2017). Rheological properties of gas and water atomized 17-4PH stainless steel MIM feedstocks: Effect of powder shape and size. *Powder technology, 312*, 152-158.

Hausnerová, B., & Sanétrník, D. (2013). Quantitative analysis of surface properties resulting from powder-binder separation. Dans *International Powder Metallurgy Congress and Exhibition, Euro PM 2013*. European Powder Metallurgy Association (EPMA).

Hausnerová, B., Sanétrník, D., & Ponizil, P. (2013). Surface structure analysis of injection molded highly filled polymer melts. *Polymer Composites, 34*(9), 1553-1558.

He, H., Li, Y., Lou, J., Li, D., & Liu, C. (2016). Prediction of density variation in powder injection moulding-filling process by using granular modelling with interstitial power-law fluid. *Powder technology, 291*, 52-59.

Heaney, D. (Éd.). (2012). *Handbook of Metal Injection Molding* (1st éd.). Woodhead Publishing.

Heaney, D., Zauner, R., Binet, C., Cowan, K., & Piemme, J. (2004). Variability of powder characteristics and their effect on dimensional variability of powder injection moulded components. *Powder metallurgy, 47*(2), 144-149.

Hidalgo, J., Abajo, C., Jimenez-Morales, A., & Torralba, J. M. (2013). Effect of a binder system on the low-pressure powder injection moulding of water-soluble zircon feedstocks. *Journal of the European Ceramic Society, 33*(15-16), 3185-3194.

Hidalgo, J., Jiménez-Morales, A., & Torralba, J. M. (2012). Torque rheology of zircon feedstocks for powder injection moulding. *Journal of the European Ceramic Society, 32*(16), 4063-4072.

http://www.finemim.com/metal-injection-molding(17-09-2018).

http://www.technocampus.be/fad/pristipim/documents/formationPRESENTIELLE-GENERALITES-indus.pdf. Repéré (17-09-2018)

https://www.lpwtechnology.com/fr/technical-library/powder-production/(20-09-2018)).

Ibrahim, R., Azmirruddin, M., Jabir, M., Johari, N., Muhamad, M., & Talib, A. (2012). Injection molding of inconel 718 parts for aerospace application using novel binder system based on palm oil derivatives. *World Academy of Science, Engineering and Technology, 70*, 526-530.

Ihle, C. F., Tamburrino, A., & Vivero, P. (2013). Effect of sample manipulation on the Couette rheometry of copper concentrates. *Powder technology, 239*, 78-85.

Ishida, H., & Rimdusit, S. (1999). Heat capacity measurement of boron nitride-filled polybenzoxazine: the composite structure-insensitive property. *Journal of thermal analysis and calorimetry, 58*(3), 497-507.

Itoh, Y., Harikou, T., Satoh, K., & Miura, H. (2002). Development of the Binder System for Solvent and Thermal Debinding in MIM Process. *Journal of the Japan Society of Powder and Powder Metallurgy, 49*(6), 518-521.

Jamaludin, K. R., Muhamad, N., Rahman, M. N. A., Ahmad, S., Ibrahim, M. H. I., & Nor, N. H. M. (2010). Rheological investigation of water atomized metal injection molding (MIM) feedstock for processibility prediction. Dans *Advanced Materials Research* (Vol. 83, pp. 945-952). Trans Tech Publ.

Jenni, M., Schimmer, L., Zauner, R., Stampfl, J., & Morris, J. (2008). Quantitative study of powder binder separation of feedstocks. *PIM Int, 2*(4), 50-55.

Jenni, M., Zauner, R., & Stampfl, J. (2009). Measurement methods for powder binder separation in PIM components. *Proceedings of EURO PM 2009, 2*, 141-146.

Kate, K. H., Enneti, R. K., Park, S.-J., German, R. M., & Atre, S. V. (2014). Predicting powder-polymer mixture properties for PIM design. *Critical Reviews in Solid State and Materials Sciences, 39*(3), 197-214.

Kowalski, L., & Duszczyk, J. (1999). Specific heat of metal powder-polymer feedstock for powder injection molding. *Journal of materials science letters, 18*(17), 1417-1420.

Kowalski, L., Duszczyk, J., & Katgerman, L. (1999). Thermal conductivity of metal powder-polymer feedstock for powder injection moulding. *Journal of materials science, 34*(1), 1-5.

Lamarre, S. G., Demers, V., & Chatelain, J.-F. (2017). Low-pressure powder injection molding using an innovative injection press concept. *International Journal of Advanced Manufacturing Technology, 91*(5-8), 2595-2605.

Leverkoehne, M., Coronel-Hernandez, J., Dirscherl, R., Gorlov, I., Janssen, R., & Claussen, N. (2001). Novel binder system based on paraffin-wax for low-pressure injection molding of metal-ceramic powder mixtures. *Advanced Engineering Materials, 3*(12), 995-998.

Leyens, C., & Peters, M. (2003). *Titanium and titanium alloys: fundamentals and applications*. John Wiley & Sons.

Li, Y.-m., Liu, X.-q., Luo, F.-h., & Yue, J.-l. (2007). Effects of surfactant on properties of MIM feedstock. *Transactions of the Nonferrous Metals Society of China, 17*(1), 1-8.

Liu, Z., Loh, N., Tor, S., & Khor, K. (2002). Characterization of powder injection molding feedstock. *Materials characterization, 49*(4), 313-320.

Majewska-Glabus, I., Zhuang, L., Vetter, R., & Duszczyk, J. (1995a). Thermal debinding of Fe3Al-X metal powder compacts. *Journal of materials science, 30*(24), 6209-6217.

Mangels, J. A., & Williams, R. M. (1983). Injection molding ceramics to high green densities.

Medvedovski, E., & Peltsman, M. (2013). Low pressure injection molding of advanced ceramic components with complex shapes for mass production. Dans *Advanced Processing and Manufacturing Technologies for Structural and Multifunctional Materials VI - 36th International Conference on Advanced Ceramics and Composites, ICACC 2012, January 22-27, 2012* (8 éd., Vol. 33, pp. 35-51). American Ceramic Society.

Mukund, B. N., Hausnerová, B., & Shivashankar, T. S. (2015). Development of 17-4PH stainless steel bimodal powder injection molding feedstock with the help of interparticle spacing/lubricating liquid concept. *Powder technology, 283*, 24-31.

Obasi, G., Ferri, O., Ebel, T., & Bormann, R. (2010). Influence of processing parameters on mechanical properties of Ti–6Al–4V alloy fabricated by MIM. *Materials Science and Engineering: A, 527*(16-17), 3929-3935.

Omar, M. A. (2001). The influence of stearic acid on the properties of injection moulding of stainless steel powder. *Journal of Technology, 10(2)*, p. 37-45.

Pengcheng, X., Fengxia, G., Zhiwei, J., Yumei, D., & Weimin, Y. (2014). Effect of gate size on the melt filling behavior and residual stress of injection molded parts. *Materials & Design, 53*, 366-372.

Poh, L., Della, C., Ying, S., Goh, C., & Li, Y. (2018). Powder distribution on powder injection moulding of ceramic green compacts using thermogravimetric analysis and differential scanning calorimetry. *Powder technology*.

Raymond, V. (2012). *Metal injection molding development: modeling and numerical simulation of injection with experimental validation* (École Polytechnique de Montréal).

Rosato 3rd, D. (2000). Injection Molding Handbook 3rd Edition Kluwer Academic Publishers Norwell: MA.

Sardarian, M., Mirzaee, O., & Habibolahzadeh, A. (2017). Influence of injection temperature and pressure on the properties of alumina parts fabricated by low pressure injection molding (LPIM). *Ceramics International, 43*(6), 4785-4793.

Sardarian, M., Mirzaee, O., & Habibolahzadeh, A. (2017a). Mold filling simulation of low pressure injection molding (LPIM) of alumina: Effect of temperature and pressure. *Ceramics International, 43*(1), 28-34.

Sardarian, M., Mirzaee, O., & Habibolahzadeh, A. (2017b). Numerical simulation and experimental investigation on jetting phenomenon in low pressure injection molding (LPIM) of alumina. *Journal of Materials Processing Technology, 243*, 374-380.

Schlechtriemen, N., Knitter, R., Haußelt, J., & Binder, J. R. (2013). Impact of powder morphology on quality of low-pressure injection moulded reaction-bonded net shape oxide ceramics. *Journal of the European Ceramic Society, 33*(4), 709-715.

Shivashankar, T. S., Enneti, R. K., Park, S.-J., German, R. M., & Atre, S. V. (2013). The effects of material attributes on powder–binder separation phenomena in powder injection molding. *Powder technology, 243*, 79-84.

Song, J., Gelin, J.-C., Barrière, T., & Liu, B. (2006). Experiments and numerical modelling of solid state sintering for 316L stainless steel components. *Journal of materials processing technology, 177*(1-3), 352-355.

Standring, T., Blackburn, S., & Wilson, P. (2016). Investigation into Paraffin Wax and Ethylene Vinyl Acetate Blends for Use as a Carrier Vehicle in Ceramic Injection Molding. *Polymer-Plastics Technology and Engineering, 55*(8), 802-817.

V. Demers, M. M. E., P. Bocher, . (2017). Moldability of low-pressure powder injection molding feedstocks. *2017 World Congress on Powder Metallurgy and Particulate Materials, PowderMet 2017, June 13, 2017 - June 16, 2017, Las Vegas, NV, United States*, pp. 401-414.

Weir, F. (1963). Moldability of plastics based on melt rheology. Part 1—theoretical development. *Polymer Engineering & Science, 3*(1), 32-36.

Yin, H., Wang, Q., Qu, X., Jia, C., & Johnson, J. L. (2011). Computational simulation and experimental analysis of the mold-filling process in μPIM. *Journal of Micromechanics and Microengineering, 21*(4), 045023.

Zaky, M. T., & Mohamed, N. H. (2010). Influence of low-density polyethylene on the thermal characteristics and crystallinity of high melting point macro-and micro-crystalline waxes. *Thermochimica acta, 499*(1), 79-84.

Zhang, M. M., & Lin, B. (2007). Simulation of ceramic injection molding for zirconia optical ferrule. Dans *Key Engineering Materials* (Vol. 336, pp. 997-1000). Trans Tech Publ.